The cell polarity scaffold Lethal Giant Larvae regulates synapse morphology and function

Jon Staples and Kendal Broadie*

Department of Biological Sciences, Kennedy Center for Research on Human Development, Vanderbilt University, Nashville, TN 37212, USA

*Author for correspondence (kendal.broadie@vanderbilt.edu)

Accepted 4 January 2013
Journal of Cell Science 126, 1992–2003

doi: 10.1242/jcs.120139

Summary

Lethal Giant Larvae (LGL) is a cytosolic cell polarity scaffold whose loss dominantly enhances neuromuscular junction (NMJ) synaptic overgrowth caused by loss of the Fragile X Mental Retardation Protein (FMRP). However, direct roles for LGL in NMJ morphological and functional development have not before been tested. Here, we use confocal imaging and two-electrode voltage-clamp electrophysiology at the *Drosophila* larval NMJ to define the synaptic requirements of LGL. We find that LGL is expressed both pre- and postsynaptically, where the scaffold localizes at the membrane on both sides of the synaptic interface. We show that LGL has a cell autonomous presynaptic role facilitating NMJ terminal branching and synaptic bouton formation. Moreover, loss of both pre- and postsynaptic LGL strongly decreases evoked neurotransmission strength, whereas the frequency and amplitude of spontaneous synaptic vesicle fusion events is increased. Cell-targeted RNAi and rescue reveals separable pre- and postsynaptic LGL roles mediating neurotransmission. We show that presynaptic LGL facilitates the assembly of active zone vesicle fusion sites, and that neuronally targeted rescue of LGL is sufficient to ameliorate increased synaptic vesicle cycling imaged with FM1-43 dye labeling. Postsynaptically, we show that loss of LGL results in a net increase in total glutamate receptor (GluR) expression, associated with the selective elevation of GluRIIB subunit-containing receptors. Taken together, these data indicate that the presynaptic LGL scaffold facilitates the assembly of active zone fusion sites to regulate synaptic vesicle cycling, and that the postsynaptic LGL scaffold modulates glutamate receptor composition and function.

Key words: Synaptogenesis, Bouton, Neurotransmission, Active zone, Synaptic vesicle cycle, Glutamate receptor, Neuromuscular junction, *Drosophila*

Introduction

Lethal Giant Larvae (LGL) was initially characterized as a *Drosophila* tumor suppressor (Gateff and Schneiderman, 1969), but has since been implicated in diverse neuronal functions, including the regulation of asymmetrical cell divisions and targeted vesicle trafficking (Ohshiro et al., 2000; Bilder et al., 2000; Wang et al., 2011a). At the *Drosophila* neuromuscular junction (NMJ), genetic interaction between *lgl* and *dfmr1* dominantly enhances the synaptic overgrowth caused by loss of the Fragile X Mental Retardation Protein (FMRP) (Zarnescu et al., 2005), a well-known translational regulator of synapse development, function and plasticity (Tessier and Broadie, 2012). LGL and FMRP also co-localize in mouse hippocampal cultures, and can be reciprocally co-immunoprecipitated from both mammalian and *Drosophila* cells (Zarnescu et al., 2005). Mammalian LGL1 selectively associates with the cortical membrane of developing axonal projections in hippocampal cultures, but is absent in developing dendrites (Wang et al., 2011a), likely reflecting conserved LGL roles in the differentiation of neuronal polarity (Rolls et al., 2003; Atwood and Prehoda, 2009; Haenfler et al., 2012). LGL1 overexpression increases axonal length, whereas RNAi knockdown causes axonal undergrowth (Wang et al., 2011a). Genetic and biochemical analyses indicate mammalian LGL1 directly interacts with Rab10 GTPase to deliver membrane vesicles to developing axonal projections (Wang et al., 2011a).

LGL is a membrane-associated scaffold that interacts with Discs Large (DLG) and Scribbled scaffolds, and apical Par6/aPKC complexes, to establish asymmetric polar determinant localization required for *Drosophila* neuroblast differentiation (Rolls et al., 2003; Atwood and Prehoda, 2009; Haenfler et al., 2012). Phosphorylation by apical aPKC disrupts the LGL binding interaction and dissociates it from the apical cortex, establishing LGL basal polarity (Betschinger et al., 2003; Betschinger et al., 2005). In mammals, the LGL1 scaffold physically interacts with myosin-IIA and the actin cytoskeleton (Betschinger et al., 2005). During active cell migration, the F-actin-associated LGL1 is cortically localized to focal adhesions where it inhibits assembly of myosin-IIA filaments (Dahan et al., 2012). Thus, LGL is a conserved membrane- and cytoskeleton-associated scaffold functioning in diverse cellular contexts to asymmetrically localize proteins and establish polarized structures. By extension, we hypothesized similar LGL mechanisms at neuronal synapses could drive the polarized vesicle delivery and molecular assemblies underlying directional structural growth and the localized exocytosis mediating neurotransmission.

In this study, we use confocal imaging and two-electrode voltage-clamp electrophysiological recording to test LGL roles in the structural and functional differentiation of the *Drosophila* glutamatergic NMJ synapse. We show LGL has a polarized distribution in motor neurons and muscles, where it is membrane-associated in pre- *and* postsynaptic compartments, respectively.

We show LGL positively regulates both synaptic morphological growth and overall neurotransmission strength, while limiting the frequency and amplitude of vesicle fusion events at individual synapses. We show that targeted RNAi and Gal4/UAS-mediated rescue of LGL function reveals separable pre- and postsynaptic requirements. Presynaptically, LGL promotes NMJ morphological growth, active zone differentiation and synaptic vesicle cycling efficacy. Postsynaptically, LGL mediates glutamate receptor (GluR) abundance and subunit composition. Together, these results establish that the membrane-associated LGL scaffold functions on both sides of the synaptic interface to modulate NMJ morphogenesis and neurotransmission strength.

Results

LGL is localized at both pre- and postsynaptic membranes of the NMJ

Null *lgl* larvae (supplementary material Fig. S1) exhibit behaviors characteristic of mutants with impaired motor function including reduced escape movement behaviors elicited by noxious heat stimuli (supplementary material Fig. S2). Null *lgl* mutants also grow much more slowly in the presence of their heterozygous siblings than when reared as fully mutant populations, suggesting impaired competitive fitness. These traits are characteristic of the large number of previously analyzed mutants with defective neuromuscular junction (NMJ) function, suggesting that LGL is likely present at the NMJ, mediating mechanisms important for functional movement output. To test this hypothesis, we first used a characterized anti-LGL antibody (Ohshiro et al., 2000; Zarnescu et al., 2005) to probe LGL expression in the neuromusculature. We confirmed antibody specificity and the loss of LGL in our array of *lgl* mutant alleles by Western blot, showing the single ~110 kDa LGL band completely eliminated in null mutants (supplementary material Fig. S1). To examine LGL expression in the neuromusculature, wandering 3rd instars were triple-labeled for LGL, the neuronal marker horseradish peroxidase (HRP) and either (1) the presynaptic active zone protein Bruchpilot (BRP) or (2) the primarily postsynaptic subsynaptic reticulum scaffold Discs Large (DLG). These data are summarized in Fig. 1.

The LGL scaffold is abundantly expressed at NMJ synapses, with little or no detectable expression outside of the synaptic domain (Fig. 1A,B). Specifically, NMJ synapses exhibit robust LGL expression that co-localizes closely with the presynaptic HRP membrane marker throughout the synaptic arbor (Fig. 1A). High magnification images of synaptic boutons show LGL within the presynaptic domain demarcated by the HRP membrane marker (white outline), in close association with BRP-marked active zones (red). LGL is detected near the presynaptic membrane and is not observed in the synaptic bouton interiors (Fig. 1A). These results suggest that LGL is membrane-associated in presynaptic boutons. Co-labeling with the postsynaptic marker DLG indicates that LGL is also present in the postsynaptic domain (Fig. 1B). LGL is clearly expressed in the muscle outside of the HRP-labeled boutons (white outline), where the protein is strongly enriched only in the NMJ perisynaptic region within the postsynaptic domains immediately apposing the synaptic boutons (Fig. 1B). LGL appears closely membrane-associated with an expression pattern largely overlapping the well-characterized postsynaptic membrane scaffold DLG (red). We conclude that LGL is enriched in the pre- and postsynaptic compartments of the NMJ, where it is membrane-associated in close proximity to BRP-labeled presynaptic active zones and DLG-labeled postsynaptic domains.

LGL promotes the growth and structural differentiation of NMJ synapses

Recent studies demonstrate a role for mammalian LGL1 in promoting axonal morphological development (Wang et al., 2011a), and aberrant synaptic morphology arises from the genetic interaction between *lgl* and *dfmr1* at the *Drosophila* NMJ (Zarnescu et al., 2005). We therefore first tested whether loss of LGL affects synaptic architecture, and observed a striking reduction in NMJ growth and complexity in null *lgl* alleles (Fig. 2A). To confirm that the structural defects were due to the loss of LGL, we used the Gal4/UAS system (Brand and Perrimon, 1993) to reintroduce wild-type LGL into the mutant ($lgl^{1/u334}$) background with the ubiquitous uh1-Gal4 driver (Rohrbough and Broadie, 2010). This transgenic expression in otherwise null mutant animals completely rescued NMJ architecture. Synaptic branches were defined as BRP/HRP positive projections consisting of ≥2 boutons. At the muscle 6/7 NMJ, the number of synaptic branches was reduced by ~50% in *lgl* mutants and was fully rescued by the uh1-Gal4 mediated rescue of LGL in the $lgl^{1/u334}$ mutant background; normalized w^{1118} control 1.00±0.08 (n=12) compared with 0.52±0.05

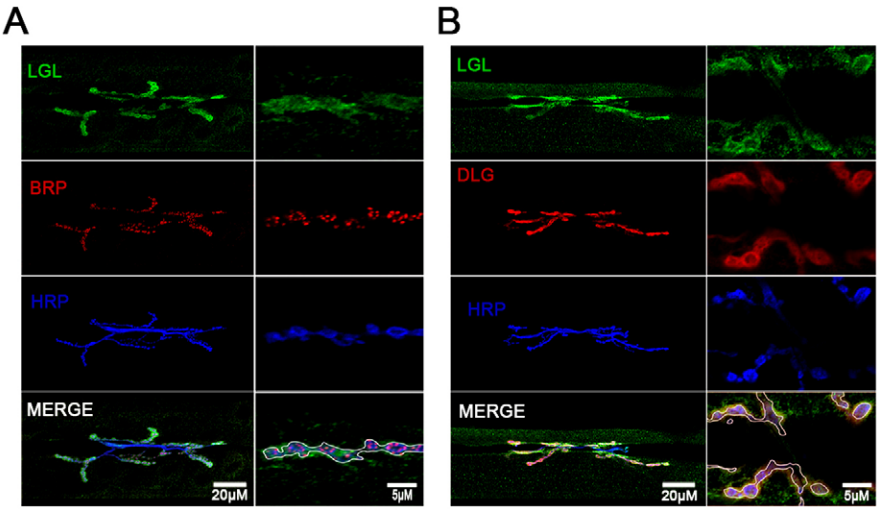

Fig. 1. LGL expression at the neuromuscular synapse. LGL antibody labeling in the wandering third instar synaptic expression at neuromuscular junctions. (**A**) Muscle 6/7 NMJ triple-labeled for LGL (green), neuronal membrane marker HRP (blue) and presynaptic active zone marker BRP (red). Low (left column) and high (right column) magnification images show LGL within the cortex of the HRP-positive presynaptic membrane (white outline; bottom right). LGL localizes near, but does not co-localize with, individual BRP active zone puncta. (**B**) Muscle 6/7 NMJ triple-labeled for LGL (green), HRP (blue) and the postsynaptic marker DLG (red). Low (left) and high (right) magnification images show LGL enriched in the postsynaptic domain, co-localizing with DLG, and also visible within the opposing HRP-positive presynaptic membrane (white outline; right).

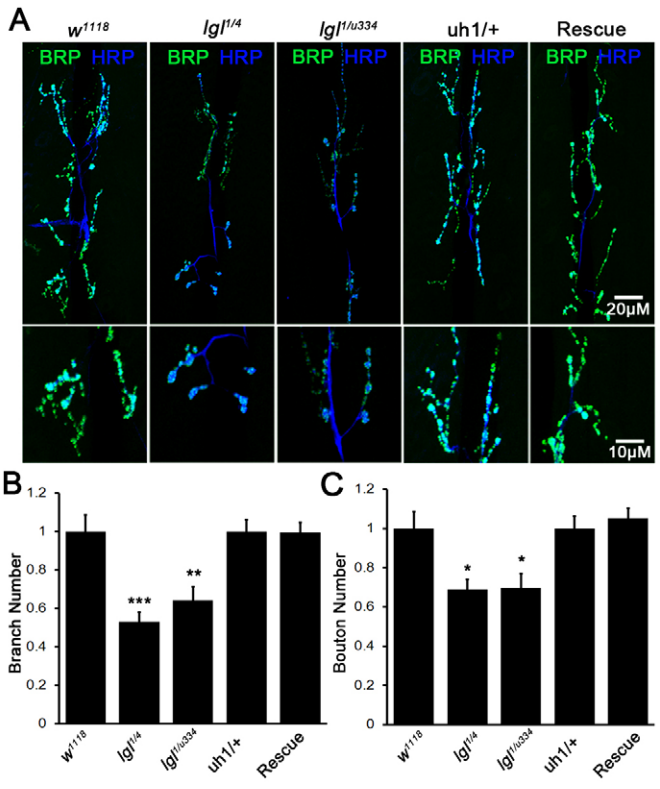

Fig. 2. LGL positively controls NMJ axonal growth and structural development. Null-*lgl* mutant NMJs exhibit a loss of axonal branches and synaptic boutons, which is rescued by transgenic expression of wild-type *lgl*. (**A**) Representative images of muscle 6/7 NMJs in genetic background control (w^{1118}), two *lgl* mutant combinations, transgenic control (uh1-Gal4/+) and uh1-Gal4 mediated UAS-*lgl* expression (UAS-*lgl*/+; $lgl^{1/u334}$; uh1-Gal4/+). Low (top) and high (bottom) magnification images show loss of NMJ structure in mutants, rescued by reintroduction of wild-type *lgl*. Synaptic boutons are defined as BRP/HRP-positive varicosities >1 μM in minimum diameter. Synaptic branches are defined as any axonal process with ≥2 boutons. (**B**,**C**) Quantification of synaptic branch number (B) and bouton number (C) for *lgl* mutant conditions versus control and transgenic rescue conditions. Sample sizes of $n=12$, 12, 12, 14 and 14 NMJs, respectively, for branch number and $n=14$, 14, 16, 16 and 14 NMJs, respectively, for bouton number. *$P<0.05$, **$P<0.01$, ***$P<0.001$.

($lgl^{1/4}$, $n=12$), and 0.64±0.07 ($lgl^{1/u334}$, $n=12$), restored back to 0.99±0.05 (uh1-Gal4 Rescue, $n=14$) compared with 1.00±0.06 (uh1-Gal4/+, $n=14$) (ANOVA $P<0.0001$; Tukey–Kramer $P<0.001$ (w^{1118} versus $lgl^{1/4}$), $P<0.01$ (w^{1118} versus $lgl^{1/u334}$), $P<0.001$ ($lgl^{1/4}$ versus uh1-Gal4) and $P<0.01$ ($lgl^{1/u334}$ versus uh1-Gal4 Rescue); Fig. 2B; see supplementary material Table S1 for all pairwise comparisons). Boutons were defined as any BRP/HRP positive puncta >1 μM in minimum diameter. Consistent with the observed branching phenotypes, the number of type I boutons was concomitantly reduced in *lgl* mutants and rescued by ubiquitous reintroduction of LGL driven by uh1-Gal4; normalized w^{1118} control 1.00±0.09 ($n=14$) compared with 0.68±0.08 ($lgl^{1/4}$, $n=14$) and 0.69±0.06 ($lgl^{1/u334}$, $n=16$), restored back to 1.05±0.06 (uh1-Gal4 Rescue, $n=14$) compared with 1.00±0.04 (uh1-Gal4/+ control, $n=16$) (ANOVA $P<0.0001$; Tukey–Kramer $P<0.05$ (w^{1118} versus $lgl^{1/4}$), $P<0.05$ (w^{1118} versus $lgl^{1/u334}$), $P<0.01$ ($lgl^{1/4}$ versus uh1-Gal4 Rescue) and $P<0.01$ ($lgl^{1/u334}$ versus uh1-Gal4 Rescue) (Fig. 2C). Thus, we demonstrate a requirement for LGL in promoting the morphological differentiation of the NMJ synapse.

We next used the Gal4/UAS system for targeted expression to determine the cell-specific requirement for LGL in synaptic morphogenesis (Fig. 3). Using the muscle-specific 24b-Gal4 driver (Brand and Perrimon, 1993) to express UAS-*lgl* (Roegiers et al., 2009) in the postsynaptic muscle cells of otherwise *lgl* null mutants, we observed improved larval motility and growth rates similar to heterozygous siblings, even when reared in competition (data not shown). At the NMJ, however, postsynaptic LGL expression provided no improvement of synaptic morphology (Fig. 3A). Axonal branch number and synaptic bouton numbers were nearly identical to the *lgl* null condition despite the dramatic behavioral improvement. The normalized mean branch number for the 24b-Gal4/+ control was 1.00±0.06 compared with 0.66±0.04 for the 24b-Gal4 postsynaptic UAS-*lgl* expression condition (Fig. 3B). Likewise, normalized bouton number for the

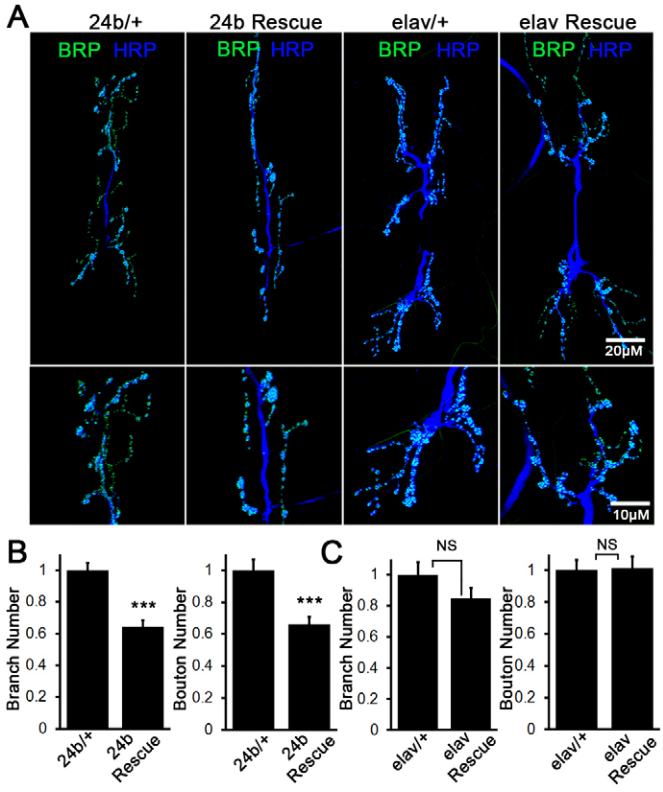

Fig. 3. Presynaptic LGL is specifically required to regulate NMJ synaptic architecture. Targeted neuronal expression of wild-type *lgl* is necessary and sufficient to rescue *lgl* NMJ mutant architecture. (**A**) Representative images of muscle 6/7 NMJs with presynaptic *elav*-Gal4 (*elav*-Gal4/UAS-*lgl*; $lgl^{1/u334}$) and postsynaptic 24b-Gal4 driven expression of *lgl* (UAS-*lgl*/+; $lgl^{1/u334}$; 24b-Gal4/+[4]) compared with controls *elav*-Gal4/+ and 24b-Gal4/+, respectively. Low (top) and high (bottom) magnification images show loss of NMJ structure in mutants, rescued by reintroduction of neuronal UAS-*lgl* only. (**B**) Quantification of synaptic branch and bouton numbers with muscle UAS-*lgl* expression versus control ($n=14$ NMJs each; branch number, Mann–Whitney test, ***$P<0.0001$; bouton number, ***$P<0.001$). (**C**) Quantification of branch and bouton numbers by neuronal UAS-*lgl* expression versus control ($n=12$ NMJs each; branch number, Mann–Whitney test, $P=0.18$; bouton number, $P=0.97$).

24b-Gal4/+ control was 1.00±0.04 compared with 0.64±0.04 for the 24b postsynaptic expression condition (n=14 each; P<0.0001, P=0.001, respectively; Mann–Whitney U-test; Fig. 3B). In striking contrast, *elav*-Gal4 (Luo et al., 1994) driven neuronal UAS-*lgl* expression effectively restored NMJ synaptic architecture comparable to wild-type levels (Fig. 3A). With targeted neuronal UAS-*lgl* expression in *lgl* null mutant animals, axonal branching was comparable to controls; normalized branch number for *elav*-Gal4/+ controls was 1.00±0.08 compared with 0.85±0.06 in the neuronal rescue condition. Likewise, the normalized bouton number for *elav*-Gal4/+ controls was 1.00±0.06 compared with 1.01±0.07 in the neuronal rescue condition [n=12 each; P=0.18, 0.89, respectively (NS); Fig. 3C]. These results show that only neuronal LGL promotes normal NMJ motor neuron growth, axonal branching and presynaptic bouton formation.

LGL strongly facilitates NMJ synaptic function

The above rescue experiments revealed an obvious disconnect between behavioral rescue and LGL roles in NMJ morphological synaptogenesis. Moreover, LGL is abundantly expressed in the muscle postsynaptic domain (Fig. 1B), yet plays no discernible role there in regulating synaptic structure. We therefore next asked whether the loss of LGL impacts NMJ neurotransmission function. Using two-electrode voltage-clamp (TEVC) electrophysiological recording, we assayed an allelic panel of *lgl* mutants, consisting of two independent homozygous null alleles (lgl^{1} and lgl^{u334}) and the heteroallelic combination of the two mutants. The TEVC configuration was used to hold constant postsynaptic muscle membrane potential while the presynaptic motor axon was electrically stimulated to induce neurotransmitter (glutamate) release. The consequent activation of ionotropic glutamate receptors alters postsynaptic muscle conductivity; recorded as the electrical current required to clamp the muscle potential. Thus, the evoked excitatory junctional current (EJC) is a broad measure of both 1) presynaptic glutamate release and 2) postsynaptic glutamate receptor activation. The results of our analysis are summarized in Fig. 4.

Loss of LGL strongly compromises neurotransmission strength at the NMJ (Fig. 4A). In all *lgl* mutant allelic combinations, there is a clear reduction in EJC transmission amplitude compared with genetic control (w^{1118}), with no significant difference between any of the mutant conditions. Importantly, ubiquitous uh1-Gal4 driven expression of UAS-*lgl* in the $lgl^{1/u334}$ mutant background completely restored the evoked EJC response to control levels (Fig. 4A). For a quantified comparison of these results between genotypes, EJC amplitude values were normalized to the w^{1118} genetic background control. Compared with the control value of 1.00±0.07 (n=10), EJC amplitudes were 0.62±0.07 (lgl^{1}/lgl^{u334}; n=10), 0.62±0.03 (lgl^{u334}/lgl^{u334}; n=7), and 0.64±0.08 (lgl^{1}/lgl^{1}; n=9) (Fig. 4B). This uniform functional defect was rescued to 1.02±0.12 (uh1-Gal4 Rescue; n=8) compared with the normalized transgenic control of 1.00±0.04 (uh1-Gal4/+ n=9) [ANOVA P<0.0001; Tukey–Kramer P<0.01 (w^{1118} versus $lgl^{1/u334}$), P<0.05 (w^{1118} versus $lgl^{u334/u334}$), P<0.05 (w^{1118} versus $lgl^{1/1}$), P<0.05 ($lgl^{1/u334}$ versus uh1-Gal4 Rescue), P<0.05 ($lgl^{u334/u334}$ versus uh1-Gal4 Rescue) and P<0.05 ($lgl^{1/1}$ versus uh1-Gal4 Rescue); Fig. 4B]. Supplementary material Table S1 shows all pairwise comparisons. Taken together, these data show that specific loss of LGL results in a ~40% reduction in NMJ neurotransmission.

We next tested whether this functional defect was pre- or postsynaptic, using both UAS-*lgl* RNAi in the wild-type background and UAS-*lgl* expression in the *lgl* null mutant background. We confirmed RNAi efficacy by Western blot, showing ubiquitous uh1-Gal4 driven knockdown completely eliminated detectable LGL protein (supplementary material Fig. S3). Using the RNAi strategy, we knocked-down LGL in presynaptic neurons with the *elav*-Gal4 driver and postsynaptically with the muscle-specific *24b*-Gal4 driver (Fig. 4A). In both cases, there was a clear decrease in synaptic transmission strength relative to controls. Moreover, neither neuron nor muscle UAS-*lgl* expression alone was able to restore normal transmission in the *lgl* null mutant. Compared with the normalized control 1.00±0.06 (*elav*-Gal4/+; n=6), the mean EJC amplitude for neuron-specific knockdown was 0.74±0.04 (*elav RNA*i; n=6) and neuron-targeted UAS-*lgl* expression 0.63±0.08 (*elav* Rescue; n=8), both highly significant reductions [ANOVA P<0.005; Newman–Keuls P<0.05

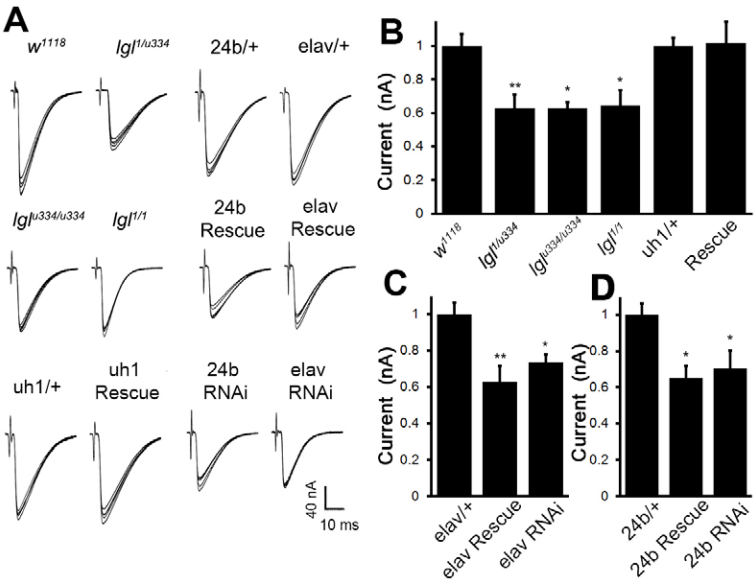

Fig. 4. LGL is required both pre- and postsynaptically for NMJ synaptic function. Two-electrode voltage-clamp (TEVC) muscle recordings of motor nerve-evoked excitatory junctional currents (EJCs) at the wandering third instar NMJ. (**A**) Representative TEVC records for the 12 genotypes shown. Each record shows five superimposed traces from an individual of each genotype. Null *lgl* mutants exhibit strong reduction in evoked synaptic response with both pre- and postsynaptic *lgl* requirements clear from target RNAi knockdown and rescue experiments. (**B**) Quantification of mean evoked EJC amplitudes in mutant compared with w^{1118} genetic control and UAS-*lgl*/+; $lgl^{1/u334}$; uh1-Gal4/+ backgrounds (n=10, 10, 7, 10, 9 and 8 NMJs, respectively). (**C**) Quantification of *elav*-Gal4 driven UAS-*lgl* expression and knockdown in motor neurons compared with the *elav*-Gal4/+ transgenic control (n=6, 6 and 8 NMJs, respectively). (**D**) Quantification of UAS-*lgl*/+; $lgl^{1/u334}$; 24b-Gal4/+ and 24b-Gal4×lgl RNAi knockdown in muscle compared with 24b-Gal4/+ transgenic control (n=8, 11 and 11 NMJs, respectively). *P<0.05, **P<0.01.

(*elav*-Gal4/+ versus *elav*-Gal4 RNAi), $P<0.01$ (*elav*-Gal4/+ versus *elav*-Gal4 Rescue) (Fig. 4C)]. Likewise, compared with the normalized muscle control 1.00±0.06 (24b-Gal4/+; $n=8$), muscle-specific knockdown amplitude was 0.70±0.10 (24b RNAi; $n=11$) and muscle-targeted UAS-*lgl* expression was 0.65±0.06; (24b Rescue; $n=11$), also both highly significant reductions [ANOVA $P<0.01$; Newman–Keuls $P<0.05$ (24b-Gal4/+ versus 24b-Gal4 RNAi), $P<0.05$ (24b-Gal4/+ versus 24b-Gal4 Rescue) (Fig. 4D)]. Taken together, these data show that LGL is required to facilitate neurotransmission in both the pre- and postsynaptic compartments, and that LGL on either side of the synapse alone is not sufficient to drive normal synaptic function.

LGL regulates spontaneous vesicle fusion frequency and amplitude

To better separate pre- and postsynaptic requirements for LGL, we next recorded miniature EJC (mEJC) events caused by the spontaneous fusion of individual synaptic vesicles with the presynaptic membrane (Long et al., 2008; Rohrbough and Broadie, 2010). The frequency of these fusion events represents presynaptic vesicle release probability, whereas mEJC amplitude represents the functional availability of the postsynaptic glutamate receptors. These data are summarized in Fig. 5. Using the same *lgl* alleles as above, we surprisingly found that both mEJC frequency and amplitude were significantly increased compared with controls (Fig. 5A). Compared with the normalized genetic control 1.00±0.07 (w^{1118}; $n=13$), mean mEJC frequency was 1.97±0.19 ($lgl^{/1u334}$; $n=9$), 1.86±0.13 ($lgl^{u334/u334}$; $n=13$) and 1.71±0.18 ($lgl^{1/1}$; $n=13$). This was a highly significant increase in mEJC frequency over control in all three *lgl* allelic combinations, with no difference between any of the mutants (Fig. 5B). Moreover, the elevated fusion frequency was completely rescued by uh1-Gal4 ubiquitous expression of LGL; 1.00±0.13 (uh1-Gal4/+; $n=8$) compared with 1.09±0.13 (uh1-Gal4 Rescue; $n=9$; Fig. 5B). Statistical comparisons between all six genotypes, as well as pair-wise analysis between all mutant and control genotypes, show these effects to be highly significant [ANOVA $P<0.0001$; Tukey–Kramer <0.001 (w^{1118} versus $lgl^{1/u334}$), $P<0.001$ (w^{1118} versus $lgl^{u334/u334}$), $P<0.01$ (w^{1118} versus $lgl^{1/1}$), $P<0.01$ ($lgl^{1/u334}$ versus uh1-Gal4 Rescue), $P<0.01$ ($lgl^{u334/u334}$ versus uh1-Gal4 Rescue) and $P<0.05$ ($lgl^{1/1}$ versus uh1-Gal4 Rescue) (Fig. 5B)]. Likewise, compared with the normalized control 1.00±0.02 (w^{1118}; $n=19$), mean mEJC amplitudes were also significantly increased in all three *lgl* mutant combinations; 1.22±0.02 ($lgl^{/1u334}$; $n=17$), 1.19±0.04 ($lgl^{u334/u334}$; $n=20$) and 1.19±0.03 ($lgl^{1/1}$; $n=18$; Fig. 5C). This defect was also full rescued by ubiquitous uh1-Gal4 expression of wild-type LGL in the null mutant background; 1.00±0.02 (uh1-Gal4/+; $n=8$) compared with 1.01±0.03 (uh1-Gal4 Rescue; $n=9$; Fig. 5C). Although the magnitude of the elevated mEJC amplitude was small, these changes were highly significant (Kruskal–Wallis $P<0.0001$; Dunn's post-test $P<0.001$ (w^{1118} versus $lgl^{1/u334}$), $P<0.01$ (w^{1118} versus $lgl^{u334/u334}$), $P<0.01$ (w^{1118} versus $lgl^{1/1}$), $P<0.01$ ($lgl^{1/u334}$ versus uh1-Gal4 Rescue), $P<0.05$ ($lgl^{u334/u334}$ versus uh1-Gal4 Rescue) and $P<0.01$ ($lgl^{1/1}$ versus uh1-Gal4 Rescue) (Fig. 5C). Taken together, these data show that specific loss of LGL results in an elevation of both presynaptic release probability and postsynaptic responsiveness.

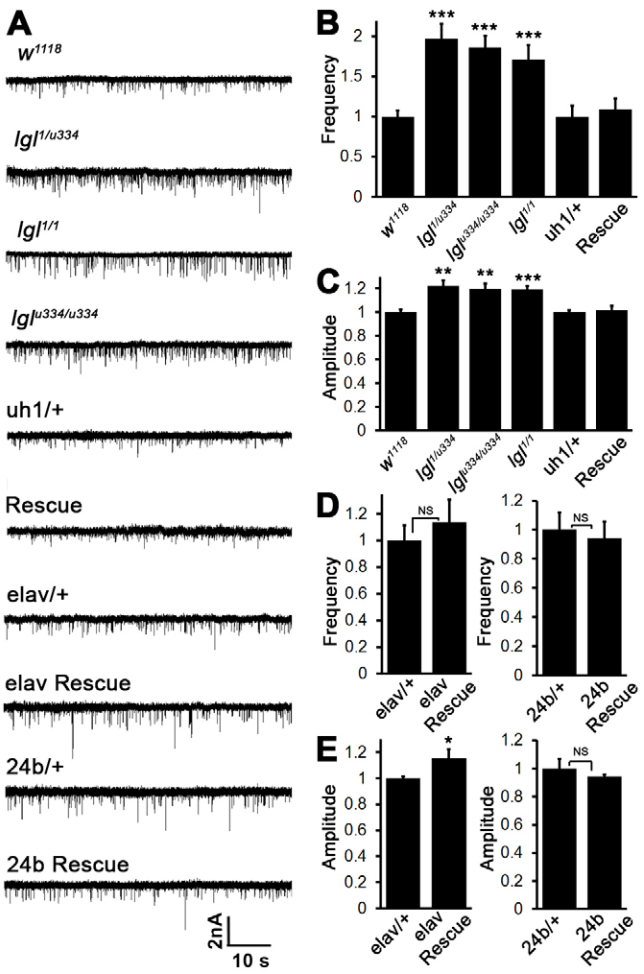

Fig. 5. LGL negatively regulates NMJ spontaneous vesicle fusion frequency and amplitude. A) Representative TEVC electrophysiological sample records (1 minute) of miniature EJC (mEJC) events for the 10 genotypes shown. Both mEJC frequency and amplitude are significantly increased in all three *lgl* mutants compared with w^{1118} control, with defects completely rescued by uh1-Gal4 driven expression of wild-type *lgl*. The pre- and postsynaptic expression of *lgl* reveals separable roles for mediating mEJC responses. (**B**) Quantification of mEJC frequency for *lgl* mutants compared with w^{1118} controls and UAS-*lgl*/+; $lgl^{1/u334}$; uh1-Gal4/+ transgenic backgrounds ($n=13$, 9, 13, 13, 8 and 9 NMJs, respectively). (**C**) Quantification of mEJC amplitude for *lgl* mutants compared with w^{1118} controls and UAS-*lgl*/+; $lgl^{1/u334}$; uh1-Gal4/+ transgenic backgrounds ($n=19$, 17, 20, 18, 8 and 9 NMJs, respectively). (**D**) Quantification of mEJC frequency for *elav*-Gal4/UAS-*lgl*; $lgl^{1/u334}$ and UAS-*lgl*/+; $lgl^{1/u334}$; 24b-Gal4/+ rescue conditions compared with GAL4 controls (*elav*-Gal4 experiments, $n=9$, and 11 NMJs; 24b-Gal4 experiments, $n=9$ and 11 NMJs). (**E**) Quantification of mEJC current amplitude for *elav*-Gal4/UAS-*lgl*; $lgl^{1/u334}$ and UAS-*lgl*/+; $lgl^{1/u334}$; 24b-Gal4/+ compared with respective controls ($n=9$ and 11 NMJs for both). NS, not significant, $*P<0.05$, $**P<0.01$, $***P<0.001$.

As with the evoked neurotransmission experiments, we next used tissue-specific UAS-*lgl* expression to test pre- versus postsynaptic cellular requirements. We found that *elav*-Gal4 driven neuronal UAS-*lgl* expression effectively restored mEJC synaptic vesicle fusion probability, but not mEJC amplitude (Fig. 5D,E). The normalized mean mEJC frequency was 1.00±0.0.11 (*elav*-Gal4/+; $n=9$) compared with 1.13±0.16

[*elav*-Gal4 rescue condition; $n=11$; $P=0.62$ (NS)], whereas normalized mEJC amplitude was 1.00±0.01 (*elav*-Gal4/+; $n=9$) compared with 1.15±0.07 (*elav*-Gal4 rescue condition; $n=11$; $^{**}P=0.01$). In intriguing contrast, UAS-*lgl* expression in the postsynaptic muscle restored both mEJC frequency and amplitude compared with the control (Fig. 5D,E). The normalized mean mEJC frequency was 1.00±0.12 (24b-Gal4/+ control; $n=9$) compared with 0.94±0.0.11 [24b-Gal4 rescue condition; $n=11$; $P=0.86$ (NS)], and mean mEJC amplitude was 1.00±0.06 (24b-Gal4/+ control; $n=9$) compared with 0.94±0.01 [24b rescue condition; $n=11$; $P=0.91$ (NS)]. Taken together, these measurements strongly support the separability of pre- and postsynaptic requirements for LGL in regulating neurotransmission function at the NMJ.

Presynaptic loss of LGL alters active zone vesicle fusion site morphology

To begin testing possible mechanisms underlying the synaptic requirement for LGL, we first examined the abundance and localization of the active zone protein Bruchpilot (BRP; Fig. 6A), a critical component of synaptic vesicle release sites (Kittel et al., 2006; Wagh et al., 2006; Fouquet et al., 2009). For quantification of paired control and mutant samples, we measured synaptic BRP immunofluorescence intensity, number of BRP active zone puncta normalized to area and BRP puncta diameter to assess active zone size. The total BRP abundance at the NMJ terminal was unchanged in all *lgl* mutants compared with control (Fig. 6A). To examine changes in distribution, BRP puncta number/area was averaged from separable puncta in type IB boutons (≥3 μM in diameter) at the muscle 6/7 NMJ, dividing by the mean bouton area. This active zone density was increased by 16–20% in *lgl* mutants over control (Fig. 6A). Compared with the normalized control 1.00±0.03 (w^{1118}; $n=12$), the *lgl* mutants were 1.20±0.04 ($lgl^{1/u334}$; $n=12$) and 1.16±0.02 ($lgl^{1/4}$; $n=12$; Fig. 6B). This change in active zones was fully rescued by uh1-Gal4 expression of LGL in the null mutant; 1.00±0.04 (uh1-Gal4/+; $n=12$) compared with 1.01±0.02 (uh1-Gal4 Rescue; $n=12$). Statistical comparisons between all genotypes and between all paired genotypes show significant differences [ANOVA $P<0.0001$; Tukey–Kramer $P<0.01$ (w^{1118} versus $lgl^{1/u334}$), $P<0.05$ (w^{1118} versus $lgl^{1/4}$), $P<0.01$ ($lgl^{1/u334}$ versus uh1-Gal4 Rescue) and $P<0.05$ ($lgl^{1/4}$ versus uh1-Gal4 Rescue) (Fig. 6B)]. Next, data were processed by the addition of a Guassian filter to a background threshold and the maximum diameter of individual BRP puncta was measured using ImageJ. The average BRP puncta diameter was found to be decreased by ~15–20% in *lgl* mutants normalized to control; 1.00±0.02 (w^{1118}; $n=12$) compared with 0.80±0.01 ($lgl^{1/4}$; $n=12$) and 0.85±0.02 (lgl^{1u3344}; $n=12$; Fig. 6C). This defect is active zone size was also rescued by uh1-Gal4 LGL expression; 1.00±0.02 (uh1-Gal4/+; $n=12$) compared with 1.01±0.02 (uh1-Gal4 Rescue; $n=12$). Statistical comparisons show the effect on active zone size to be highly significant [ANOVA $P<0.0001$; Tukey–Kramer $P<0.001$ (w^{1118} versus $lgl^{1/4}$), $P<0.001$ (w^{1118} versus $lgl^{1/u334}$), $P<0.01$ ($lgl^{1/4}$ versus uh1-Gal4 Rescue) and $P<0.001$ ($lgl^{1/u334}$ versus uh1-Gal4 Rescue) (Fig. 6C)]. Taken together, these data show that specific loss of LGL changes active

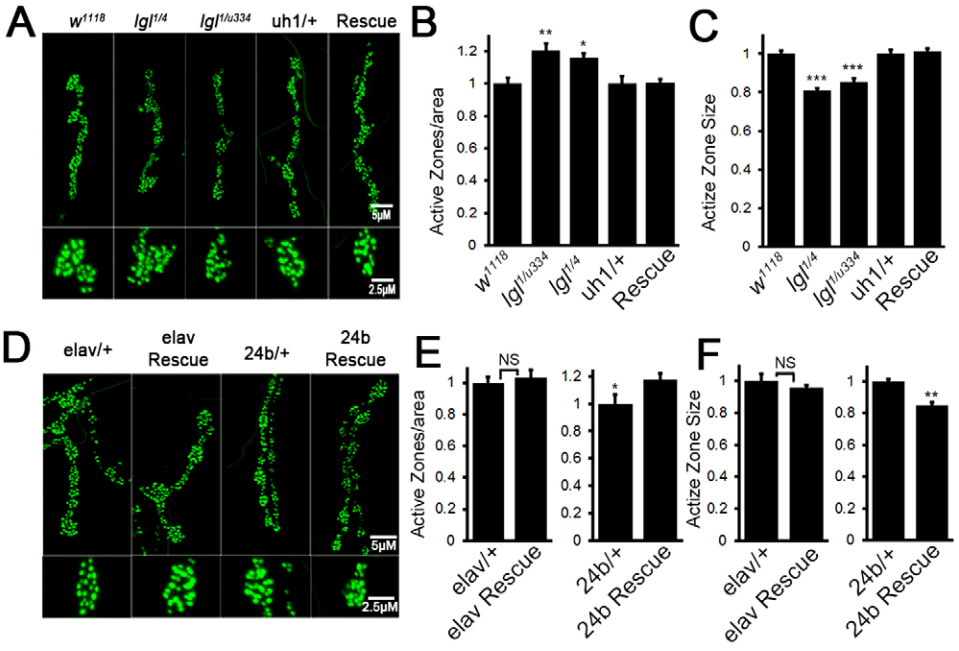

Fig. 6. LGL regulates presynaptic active zone organization. (**A**) Representative images of NMJ presynaptic active zones labeled with anti-BRP (NC82; green) in matched control and *lgl* mutant conditions, with uh1-Gal4/+ control and ubiquitous expression of wild-type *lgl* in the $lgl^{1/u334}$ mutant background. Lower panel shows higher magnification images of the BRP puncta in each of the five genotypes. (**B**) Quantification of BRP puncta/area in *lgl* mutant conditions compared with w^{1118} and UAS-*lgl*/+; $lgl^{1/u334}$; uh1-Gal4/+ backgrounds ($n=12$ NMJs each). (**C**) Quantification of BRP diameter in *lgl* mutant conditions compared with w^{1118} and UAS-*lgl*/+; $lgl^{1/u334}$; uh1-Gal4/+ backgrounds ($n=12$, 12, 12, 12 and 12 NMJs, respectively). (**D**) Representative low (top) and high (bottom) magnification images of BRP-labeled active zone size and density in *elav*-Gal4/UAS-*lgl*; $lgl^{1/u334}$ and UAS-*lgl*/+; $lgl^{1/u334}$; 24b-Gal4/+ rescue conditions compared with respective controls. (**E**) Quantification of BRP puncta/area in *elav*-Gal4/UAS-*lgl*; $lgl^{1/u334}$ and UAS-*lgl*/+; $lgl^{1/u334}$; 24b-Gal4/+ conditions ($n=10$ NMJs each). (**F**) Quantification of BRP puncta size in *elav*-Gal4/UAS-*lgl*; $lgl^{1/u334}$ and UAS-*lgl*/+; $lgl^{1/u334}$; 24b-Gal4/+ conditions ($n=12$ NMJs each). NS, not significant, $^{*}P<0.05$, $^{**}P<0.01$, $^{***}P<0.001$.

zone organization by increasing the average density but decreasing the average size of synaptic vesicle release sites.

Since total BRP levels were unchanged in *lgl*-null mutants, the above results indicate a LGL role in the localization/aggregation of the synaptic vesicle release machinery. We next wished to test whether this LGL role is cell-autonomous within the motor neurons, or results as a consequence or *trans*-synaptic signaling or compensation. A cell-autonomous requirement in the presynaptic neuron was found because targeted neuronal expression of wild-type LGL rescued active zone defects in *lgl* mutants, whereas postsynaptic muscle LGL expression had no impact on the mutant phenotypes (Fig. 6D). In these rescue experiments, the normalized mean BRP puncta number/area was 1.00±0.07 in control (*elav*-Gal4/+; $n=10$) compared with 1.03±0.03 with targeted neuronal expression [*elav*-Gal4 rescue condition; $n=10$; $P=0.62$ (NS); Mann–Whitney U-test; Fig. 6E], whereas the active zone size was 1.00±0.06 in control (24b-Gal4/+) compared with 1.17±0.04 with targeted muscle expression (24b-Gal4 Rescue; $n=12$; $P=0.03$; Mann–Whitney U-test; Fig. 6F). Likewise, normalized BRP puncta size was 0.95±0.01 [*elav*-Gal4 rescue condition; $n=10$; $P=0.33$ (NS); Mann–Whitney U-test; Fig. 6E] and 0.85±0.01 (24b-Gal4 rescue condition; $n=12$; $P<0.01$; Mann–Whitney U-test1; Fig. 6F). Thus, there is a clear presynaptic role for the LGL scaffold in mediating the clustering/aggregation of active zone synaptic vesicle release sites, correlating with the presynaptic functional requirement for LGL in the regulation of neurotransmission strength.

LGL modulates synaptic vesicle cycling efficacy

The changes in presynaptic active zones predict possible alterations in the synaptic vesicle cycling underlying neurotransmission defects in *lgl* mutants. This is also a particularly important mechanistic question because removal of presynaptic LGL reduces evoked neurotransmission strength for the entire NMJ (Fig. 4), yet increases in the frequency of vesicle fusion at individual active zones (Fig. 5). To test synaptic vesicle cycling in *lgl* mutants, we used the lipophilic dye FM1-43 to visualize endo/exocytosis (Fig. 7; Huang et al., 2006; Long et al., 2008; Vijayakrishnan et al., 2009). The muscle 6/7 NMJ was exposed to 10 μM FM1-43 in saline containing 90 mM KCl, to depolarize the synaptic terminal and label endocytosed synaptic vesicles (Fig. 7A, load). Quantified comparisons showed that the fluorescent intensity of loaded terminals was unchanged in *lgl* mutants normalized to the w^{1118} control; 1.04±0.05 ($lgl^{1/4}$; $n=10$) and 0.98±0.04 [$lgl^{1/u334}$; $n=14$; ANOVA $P=0.76$ (NS); Fig. 7B]. The efficacy of synaptic vesicle exocytosis was next determined by a second depolarization in the absence of FM1-43 (Fig. 7A, unload). In this case, the unloaded fluorescent intensity was significantly reduced by ~20–24% in *lgl* mutants normalized to control; 0.76±0.05 ($lgl^{1/4}$; $n=10$; $P=0.01$) and 0.80±0.04 ($lgl^{1/u334}$; $n=14$; Fig. 7C). Statistical comparisons confirmed a significant change between all genotypes and in pair-wise combinations [ANOVA $P=0.02$; Newman–Keuls $P<0.05$ (w^{1118} versus $lgl^{1/4}$), $P<0.05$ (w^{1118} versus $lgl^{1/u334}$) (Fig. 7C)]. The ratio of unloaded/loaded intensity normalized to control was 0.73±0.05 ($lgl^{1/4}$; $n=10$) and 0.84±0.04 ($lgl^{1/u334}$; $n=14$; Fig. 7D). This confirmed a significantly increased synaptic vesicle cycling rate in the absence of LGL [ANOVA $P=0.008$; Newman–Keuls $P<0.01$ (w^{1118} versus $lgl^{1/4}$), $P<0.05$ (w^{1118} versus $lgl^{1/u334}$) (Fig. 7D)]. We further found that targeted neuronal expression of wild-type UAS-*lgl* was sufficient to rescue the observed mutant defect in vesicle cycling. Compared with the normalized control (*elav*-Gal4/+; $n=10$), the unloaded/loaded intensity ratio was 0.94±0.05 in the *elav* rescue condition ($n=10$; $P=0.68$), showing rescue of the defect (Wilcoxon matched-pairs test; Fig. 7E). Together these data demonstrate that synaptic vesicle cycling is significantly elevated in the absence of presynaptic LGL.

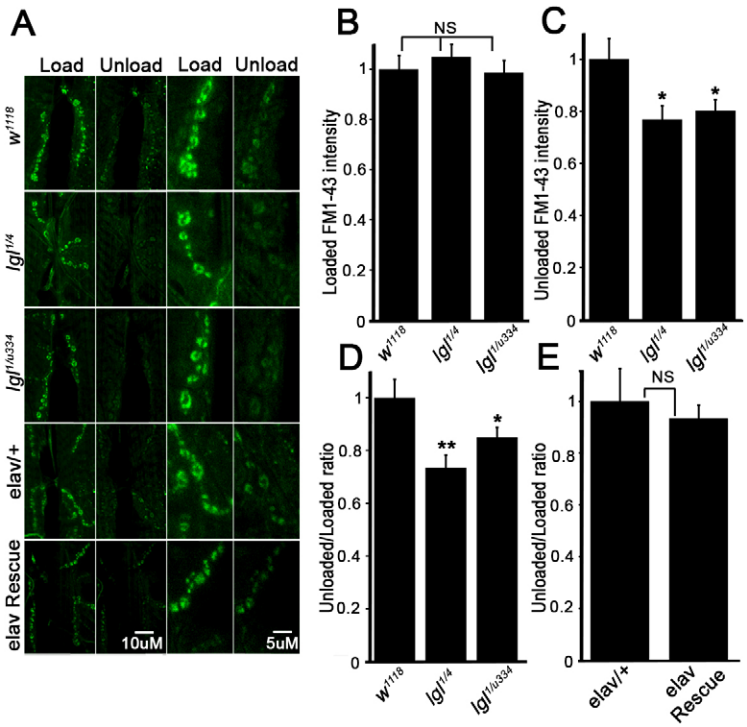

Fig. 7. LGL regulates synaptic vesicle cycling rate in NMJ presynaptic boutons. Loss of LGL causes increased cycling of FM1-43 lipophillic dye that is rescued by neuronally targeted wild-type UAS-*lgl* expression. (**A**) Low (left two columns) and high (right two columns) magnification images of FM1-43-labeled muscle 6/7 NMJs following depolarization-dependent loading and unloading in the five indicated genotypes. (**B**) Quantification of normalized loaded FM1-43 intensity. There is no significant change for the *lgl* mutants compared with control ($n=14$, 10 and 14 NMJs; ANOVA, $P=0.76$). (**C**) Quantification of FM1-43 unloaded intensity. Both *lgl* mutants unload more dye compared with control ($n=14$, 10 and 14 NMJs respectively; ANOVA, $P=0.02$). (**D**) Ratio of Loaded/unloaded fluorescent intensity ($n=14$, 10 and 14 NMJs respectively; ANOVA, $P=0.008$). (**E**) Quantification of the *elav*-Gal4/+ transgenic control compared with *elav*-Gal4/UAS-*lgl*; $lgl^{1/u334}$ expression condition ($n=10$ NMJs each; $P=0.68$, which is not significant, Wilcoxon matched-pairs test). NS, not significant, *$P<0.05$, **$P<0.01$.

Postsynaptic LGL regulates glutamate receptor abundance and subunit composition

In addition to presynaptic requirements, the LGL scaffold is abundantly present at the postsynaptic membrane (Fig. 1), where it modulates evoked neurotransmission strength (Fig. 4) and postsynaptic responsiveness to spontaneous vesicle fusion events (Fig. 5). These results strongly predict alterations in the postsynaptic glutamate receptor (GluR) domains in *lgl* mutants. To test this hypothesis, we used immunocytochemistry to analyze both overall GluR abundance and subunit composition. NMJ ionotropic GluRs are thought to be tetrameric, consisting of 3 essential subunits (GluRIIC, D and E) and a fourth variable subunit, GluRIIA or GluRIIB (DiAntonio et al., 1999; Marrus et al., 2004; Featherstone et al., 2005). Subunits A and B compete for inclusion within the tetramer complex and confer distinct physiological characteristics to the channel (DiAntonio et al., 1999). It has been established that the two GluR classes are regulated independently. For example, FMRP in conjunction with *Drosophila* metabotropic glutamate receptor A (DmGluRA) differentially regulates the expression of GluRIIA versus GluRIIB (Pan and Broadie, 2007), and the membrane scaffold DLG, a target of FMRP translational repression (Darnell et al., 2011), selectively regulates only GluRIIB and not GluRIIA (Chen and Featherstone, 2005). To test total GluRs and each GluR class, we used specific antibody probes for the common GluRIIC subunit (total GluRs), and the differential GluRIIA and GluRIIB subunits, to compare *lgl* mutants to controls and transgenic conditions. These data are summarized in Fig. 8; enlarged panels of Fig. 8 are available in supplementary material Fig. S4 and Fig. S5.

We first used an affinity-purified antibody specific to the essential GluRIIC subunit (Marrus et al., 2004; Rohrbough and Broadie, 2010) to measure total GluR abundance in the NMJ postsynaptic domains (Fig. 8A). Consistent with the observed LGL role in regulating transmission strength and the increase in *lgl* mutant mEJC amplitudes, we observed an >40% increase in GluRIIC immunofluorescence intensity in *lgl* mutants normalized to w^{1118} genetic background control; 1.43±0.05 ($lgl^{1/4}$; n=12) and 1.42±0.05 ($lgl^{1/u334}$; n=12) (Fig. 8B). This total GluR increase was restored to control levels by uh1-Gal4 driven UAS-*lgl* expression in the otherwise null mutant background; 1.07±0.03 (uh1-Gal4 Rescue; n=13) (Fig. 8B). Statistical comparisons between all genotypes and in post-test pairwise combinations showed significant changes (Kruskal–Wallis P<0.0001; Dunn's post-test P<0.001 (w^{1118} versus $lgl^{1/4}$), P<0.001 (w^{1118} versus $lgl^{1/u334}$), P<0.05 ($lgl^{1/4}$ versus uh1-Gal4 Rescue) and P<0.05 ($lgl^{1/u334}$ versus uh1-Gal4 Rescue) (Fig. 8B). Taken together, these data show that specific loss of LGL elevates total glutamate receptor abundance at the NMJ.

Testing cellular requirements for LGL in GluR regulation, we found a cell-autonomous postsynaptic role (Fig. 8A). Targeted postsynaptic LGL expression was necessary and sufficient to rescue GluRIIC expression to control levels, whereas presynaptic LGL had no effect on the *lgl* mutant phenotype. Normalized GluRIIC levels remained elevated at 1.34±0.09 with neuronal *elav*-Gal4 driven UAS-*lgl* expression (n=12; P=0.03; Mann–Whitney U-test; Fig. 8C), but was restored to 0.99±0.06 with postsynaptic muscle 24b-Gal4 driven UAS-*lgl* rescue [n=14; P=0.97 (NS); Mann–Whitney U-test; Fig. 8D]. We next tested GluR subunit composition using GluRIIA and GluRIIB antibodies (Fig. 8E). Intriguingly, GluRIIA abundance at *lgl* mutant synapses was not significantly different from controls, whereas GluRIIB level was increased by approximately the same fold as total GluRIIC (Fig. 8E). The normalized GluRIIA intensity was 0.90±0.05 ($lgl^{1/4}$; n=12) and 0.95±0.06 [$lgl^{1/334}$; n=12; ANOVA P=0.62 (NS); Fig. 8F], whereas GluRIIB intensity was 1.36±0.09 ($lgl^{1/4}$; n=12) and 1.31±0.09 [$lgl^{1/334}$;

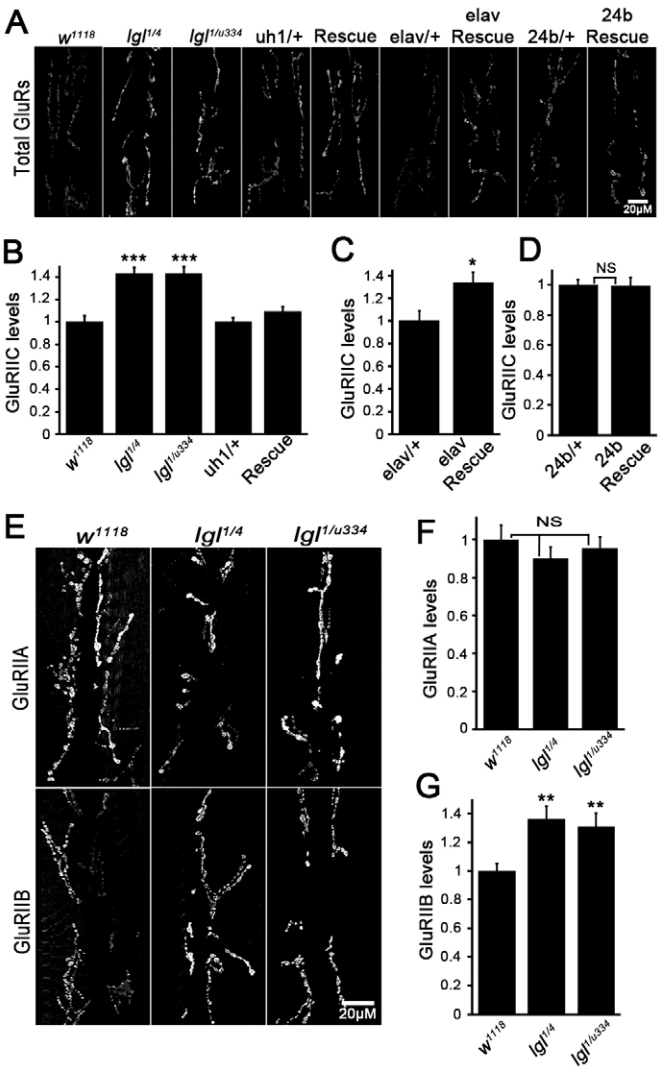

Fig. 8. LGL regulates postsynaptic glutamate receptor abundance and subunit composition. Loss of LGL induces a net increase in total glutamate receptors (GluRs) caused by the selective elevation of GluRIIB-containing receptors at wandering third instar NMJ synapses. (**A**) Representative muscle 6/7 NMJ images of anti-GluRIIC labeling in control (w^{1118}) and *lgl* mutant backgrounds, with ubiquitous, neuronal- and muscle-driven UAS-*lgl* expression. (**B**) Quantification of GluRIIC labeling intensity in w^{1118} and UAS-*lgl*/+; $lgl^{1/u334}$; uh1-Gal4/+ backgrounds compared with *lgl* mutants (n=12, 12, 12, 13 and 13 NMJs, respectively; Kruskal–Wallis P<0.0001). (**C**) Quantification of GluRIIC intensity in the *elav*-Gal4/+ control versus UAS-*lgl* expression condition (n=12 NMJs each; P=0.03, Mann–Whitney test). (**D**) Quantification of GluRIIC intensity in 24b-Gal4/+ control versus UAS-*lgl*/+; $lgl^{1/u33}$; 24b-Gal4/+ condition (n=14; P=0.88). (**E**) Representative NMJ 6/7 images of anti-GluRIIA/B labeling in control and *lgl* mutants. (**F**) Quantification of GluRIIA intensity in control and *lgl* mutant backgrounds (n=12 NMJs each; ANOVA, P=0.62, which is not significant). (**G**) Quantification of GluRIIB intensity in control and *lgl* mutants (n=12 NMJs each; ANOVA, P=0.005). NS, not significant, *P<0.05, **P<0.01, ***P<0.001.

$n=12$; ANOVA $P=0.005$; Newman–Keuls $P<0.01$ (w^{1118} versus $lgl^{1/4}$) and $P<0.01$ (w^{1118} versus $lgl^{1/u334}$)] (Fig. 8G). Taken together, these data indicate that the postsynaptic LGL scaffold is specifically required to regulate the localization of GluRIIB-containing receptors, and that the observed increase in total GluR abundance in *lgl* mutants is due to an increase in GluRIIB class receptors.

Discussion

Lethal Giant Larvae (LGL) is a well-characterized scaffolding protein with numerous WD40 protein–protein and cytoskeletal interaction domains, which functions in polarized protein recruitment to localized cellular compartments. Defined first as a tumor suppressor (Gateff and Schneiderman, 1969), LGL has been studied primarily in asymmetrical cell fate determinant localization during neural stem cell division (Bilder et al., 2000; Ohshiro et al., 2000; Betschinger et al., 2005; Atwood and Prehoda, 2009; Ogawa et al., 2009; Haenfler et al., 2012). In addition, loss of LGL has also long been known to dominantly enhance the loss of Fragile X Mental Retardation Protein (FMRP) in control of NMJ architecture (Zarnescu et al., 2005). Recently, mammalian LGL1 was shown to directly interact with Rab10 GTPase in polarized delivery of membrane-precursor vesicles to distal axonal projections (Wang et al., 2011a). Based on these observations, we asked whether LGL might control synaptic morphogenesis and neurotransmission, using the well-characterized *Drosophila* NMJ synapse model. Here, we report clearly separable pre- and postsynaptic roles for the LGL scaffold in axonal growth, branching and bouton formation; organization and function of presynaptic active zones; and the composition and function of postsynaptic glutamate receptors. Together, these LGL activities strongly modulate neurotransmission strength.

In *Drosophila* larvae, LGL displays strong expression in NMJ synapses, where it closely overlaps with the well-characterized DLG synaptic scaffold. Interestingly, both LGL and DLG scaffolds localize basal determinants in embryonic neuroblasts (Bilder et al., 2000; Ohshiro et al., 2000; Atwood and Prehoda, 2009; Ogawa et al., 2009; Haenfler et. al., 2012) and, consistently, both scaffolds are similarly enriched in the muscle postsynaptic domain and neuronal presynaptic boutons, tightly associated with the membrane cortex on both sides of the synaptic interface. Global LGL loss reduces NMJ architectural complexity, with fewer axonal branches and synaptic boutons, which is rescued by neuron specific LGL expression, paralleling the presynaptic cell-autonomous FMRP requirement in synaptic morphogenesis (Gatto and Broadie, 2008). Global LGL loss also causes a ~40% decrease in neurotransmission strength, but this requirement has both pre- and postsynaptic elements. LGL negatively regulates the frequency and amplitude of spontaneous synaptic vesicle fusion events, and likewise controls these properties in separable pre- and postsynaptic roles. Presynaptic loss of LGL cell-autonomously alters the density and size of BRP-containing active zones, although total BRP levels are unchanged, indicating a localization function. Similarly, postsynaptic loss of LGL causes a cell-autonomous increase in GluR localization, correlated with the selective upregulation of GluRIIB-containing receptors. Together, these data demonstrate distinct scaffolding requirements for LGL on either side of the NMJ synapse. Since mammalian FMRP binds LGL1 mRNA (Darnell et al., 2011), these results suggest a possible regulatory pathway controlling synaptic modulation.

Classical interpretations of miniature event records suggest frequency reflects presynaptic fusion probability, amplitude reflects the number/function of postsynaptic receptors, and that these properties additively predict evoked neurotransmission strength (Fatt and Katz, 1952; Cull-Candy and Miledi, 1982). Miniature event recordings of *lgl*-null synapses indicate increased presynaptic vesicle fusion probability and postsynaptic glutamate receptor number but, conversely, evoked records show a strong reduction in neurotransmission. Our FM1-43 data show elevated vesicle cycling at the individual bouton level, which is consistent with the increased mEJC frequency. Although the mEJC and FM1-43 data seemingly contradict our EJC records, the simplest interpretation is that increased neurotransmission at the individual bouton level is simply insufficient to compensate for the severe loss of bouton numbers in *lgl* mutants. Alternatively, many studies indicate that the relationship between spontaneous and evoked vesicle release may not be straightforward (Sara et al., 2005; Mathew et al., 2008; Fredj and Burrone, 2009; Chung et al., 2010), and there are numerous precedents for a similar disconnect. For example, loss of the Synaptotagmin calcium sensor causes increased spontaneous vesicle fusion, but a dramatic decrease in evoked response (Broadie et al., 1994; Xu et al., 2009). Similarly, loss of Fuseless (Fusl), a protein required for presynaptic calcium channel localization, simultaneously causes increased mEJC frequency and decreased evoked transmission (Long et al., 2008). Likewise, LGL may function to differentially regulate spontaneous and evoked transmission events. As LGL binds both membrane-associated proteins and actin cytoskeleton (Betschinger et al., 2005), and acts to asymmetrically localize proteins (Atwood and Prehoda, 2009; Ogawa et al., 2009; Fletcher et al., 2012; Haenfler et. al., 2012), we propose LGL similarly regulates neurotransmission by controlling growth and localizing/clustering membrane-associated vesicle release machinery (e.g. BRP). Intriguingly, *Drosophila* Rab3 GTPase also regulates presynaptic BRP-containing active zone morphology (Graf et al., 2009). Although Rab3 loss results in the opposite defects to loss of LGL, this relationship may have some bearing on the recently defined interaction between mammalian LGL1 and Rab10 GTPase (Wang et al., 2011a).

In the postsynaptic domain, both mEJC recordings and GluR immunolabeling indicate that total glutamate receptor abundance is increased in *lgl* mutants, driven by selective recruitment of GluRIIB-containing receptors. This GluR shift may have important functional consequences, as single channel recordings show that GluRIIB-containing receptors repolarize nearly 10 times faster than GluRIIA-containing receptors (DiAntonio et al., 1999; Marrus et al., 2004), and evoked neurotransmission is strongly attenuated at NMJs containing only GluRIIB rather than GluRIIA channels (Schmid et al., 2008). In addition, these two GluR classes differentially regulate *trans*-synaptic signaling. For example, GluRIIA overexpression causes increased synaptic boutons, postsynaptic densities and presynaptic T-bar active zones, whereas the inverse changes occur with GluRIIB overexpression (Sigrist et al., 2002). Several studies indicate that GluRIIA selectively acts in a PKA/cAMP-dependent retrograde *trans*-synaptic signaling pathway that modulates presynaptic release properties (Petersen et al., 1997; Davis et al., 1998; Sigrist et al., 2002; Yoshihara et al., 2005). During NMJ synaptogenesis, postsynaptic sites appear initially GluRIIA-enriched, but acquire more GluRIIB during maturation, and

alterations of this ratio are activity-dependent (Schmid et al., 2008). We show here that LGL is specifically required to inhibit postsynaptic localization of GluRIIB-containing receptors, and thereby liklely modulates synaptic functional properties, as well as the potential for *trans*-synaptic signaling. Intriguingly, the LGL-associated DLG scaffold similarly regulates only GluRIIB-containing receptors (Chen and Featherstone, 2005). Moreover, genetically-interacting FMRP also differentially regulates GluRIIB at the *Drosophila* NMJ (Pan and Broadie, 2007), and mammalian FMRP binds the mRNA of both LGL1 and the DLG homologue, PSD95 (Darnell et al., 2011). The co-localization of LGL and DLG in the postsynaptic domain, their known direct interaction, their common regulation by FMRP, and the common role regulating GluRIIB-containing receptors (Ohshiro et al., 2000; Chen and Featherstone, 2005), all suggest a mechanism for selective control of this specific GluR class.

Although almost all of our data indicate strict cell-autonomous pre- and postsynaptic LGL requirements, we also show that LGL facilitates a retrograde *trans*-synaptic signal. Specifically, postsynaptic expression of LGL restores synaptic vesicle fusion probability and response amplitude to control levels, while presynaptic LGL expression restores only mEJC frequency. Moreover, while targeted pre- and postsynaptic RNAi against LGL shows clearly separable roles in neurotransmission, the loss of evoked synaptic current amplitude cannot be rescued by reintroduction of LGL into either pre- or postsynaptic cell alone, but requires LGL on both sides of the synapse. A possible mechanistic link is the known interaction between LGL and the *trans*-synaptic signal Wingless (Wg), the founding *Drosophila* Wnt protein (Mann, 1923; Waddington, 1940; Sharma, 1973). Indeed, Disheveled (Dsh) and Frizzled-8 (Fz8) Wnt receptors are required to localize vertebrate LGL to the cortex of *Xenopus* embryos (Dollar et al., 2005), in a manner similar to the Par6/aPKC-mediated basolateral localization of LGL required for the asymmetrical division of *Drosophila* neuroblasts (Rolls et al., 2003; Betschinger et al., 2003; Atwood and Prehoda, 2009; Haenfler et. al., 2012). Similar signaling mechanisms may also control synaptic development. Considerable evidence shows polarity proteins required for neuroblast differentiation continue to function during synaptogenesis, including aPKC/Par6/PP2A, LGL/DLG/Scribbled and Wg/Dsh/Fz (Zhang et al., 2007a; Zhang et al., 2007b; Ramachandran et al., 2009; Viquez et al., 2009; Mosca and Schwarz, 2010; Wang et al., 2011a; Wang et al., 2011b). Given the breadth of studies linking these proteins to NMJ synaptogenesis, and established links to FMRP regulation, it appears likely that these 'polarity proteins' may also mediate polarized synaptic assembly downstream of FMRP translational control.

This study is the first *in vivo* characterization of synaptic requirements for the membrane-associated LGL scaffold, demonstrating roles in modulating both synaptic architecture and neurotransmission strength. LGL requirements are largely separable into distinct pre- and postsynaptic cell-autonomous roles, both of which strongly impact the efficacy of neurotransmission. These synaptic modulatory functions are strongly reinforced by the long-known interactions between 1) LGL and FMRP (Zarnescu et al., 2005), an RNA-binding translational regulator of activity-dependent changes in synaptic structure/function (Tessier and Broadie, 2009); 2) LGL and DLG, likewise a tumor suppressor and cell-polarity scaffold (Ohshiro et al., 2000) with critical roles controlling synaptic architecture/function (Mathew et al., 2002; Zhang et al., 2007a; Wang et al., 2011b); and 3) LGL and the Wnt/Wg signaling pathway, also a key regulator of cell polarity and synaptic structure/function (Dollar et al., 2005; Miech et al., 2008; Korkut et al., 2009). Although many of these interactions remain to be explored in the synaptic context, this study provides enticing evidence that LGL may link synaptic translational regulation and the directional localization of encoded proteins to signaling complexes on both sides of the synaptic cleft.

Materials and Methods

Genetic stocks

All *lgl* mutant alleles were maintained as GFP-balancer stocks, including *w*; lgl^{u334}/*CyO*KrGFP, *w*; lgl^{1}/*CyO*KrGFP and *w*; lgl^{4}/*CyO*KrGFP. The lgl^{u334} allele is a strong hypomorph containing a 10 kb deletion of the telomeric and regulatory regions upstream of the *lgl* locus, which maps to the proximal region of chromosome 2L (Mechler et al., 1985). The lgl^{4} and lgl^{1} lesions are characterized as full loss-of-function null alleles containing 22 kb and 18 kb deletions of the *lgl* locus, respectively (Mechler et al., 1985; Zarnescu et al., 2005; Betschinger et al., 2006). Western blot analysis confirmed that both lgl^{1} and lgl^{4} show no detectable LGL expression, whereas trace amounts of LGL were present in the lgl^{u334} line, consistent with a strong hypomorph (supplementary material Fig. S1). Phenotypically, lgl^{4} larvae were developmentally retarded and consistently smaller than either lgl^{1} or lgl^{u334}, and were therefore not used in the homozygous condition. All experiments using transheterozygous allelic combinations were generated from virgin female *w*; lgl^{1}/*CyO*KrGFP, and all genetic background control experiments were performed using a *w* line derived from the lgl^{1} null background. RNAi experiments were performed using a *w*; *lgl*-RNAi/*lgl*-RNAi line (w; P{GD4047}v51247; Dickson et al., 2007) crossed to either the muscle-specific Gal4 driver *24b* (*w*; *24b*-Gal4/*24b*-Gal4; Brand and Perrimon, 1993; Nitabach et al., 2006; Rohrbough and Broadie, 2010) or the neuron-specific Gal4-driver *elav* (*w*; *elav*-Gal4/y; Luo et al., 1994; Rohrbough and Broadie, 2010). Rescue experiments were done on lines generated from a cross between UAS-*lgl*; lgl^{u334}/*CyO*KrGFP males (Roegiers et al., 2009), and virgin females from (1) lgl^{1}/croKrGFP; uh1-Gal4 for ubiquitous expression (w; +; uh1-Gal4; Wodarz et al., 1995), (2) lgl^{1}/*CyO*KrGFP; 24b-Gal4 for muscle expression or (3) *elav*-Gal4; lgl^{1}/*CyO*KrGFP for neuronal expression. To control for background effects of Gal4 drivers, a single copy of each Gal4 driver alone was crossed into the *lgl* control background (uh1-Gal4/+, 24b-Gal4/+ and *elav*-Gal4/+). All animals were reared at 25℃ in a 12/12 light/dark cycle on standard food.

Behavioral assay

To assess motor activity in wandering third instar larvae, we used the well-characterized escape movement behavior elicited in response to noxious thermal stimulation (Tracey et al., 2003). The stereotyped rolling response requiring highly coordinator motor function was assayed as described previously (Tracey et al., 2003). In brief, a small probe heated to a constant 45℃ using a variac powersource and monitored with a digital thermometer was applied to the larval body-wall medial at hemisegments 3 and 4. Behavioral responses were recorded with a Canon Rebel T3 digital camera for 10 seconds from stimulus onset. Movement responses were categorized as fast (≤1 seconds), slow (2–10 seconds) or no response (≥10 seconds). In total, 60 w^{1118} control and 54 *lgl* mutant larvae were tested, and the data were analyzed by a 2×3 Chi^2 test of independence.

Immunocytochemistry

Adult flies were induced to lay for 24 hours at 25℃ on apple juice/agar plates with nutritional supplementation provided by a yeast and water paste. 30 size-matched larvae of each genotype were selected at 48 hours and transferred to a fresh supplemented agar plate. We observed that *lgl* mutant larvae grew at rates similar to controls in the absence of their heterozygous cohorts. Wandering 3rd instars were collected and size matched to controls for all comparative analyses. Larvae were dissected in physiological saline (see the Electrophysiology section), fixed in ice-cold methanol (GluR studies) or 4% paraformaldehyde (all other markers) for 5 minutes, and then washed 2×20 minutes in 0.3% PBST (PBS+0.3% Tween). Antibody probes used included: affinity-purified LGL antibody (rabbit anti-LGL, 1:500; Ohshiro et al., 2000; Zarnescu et al., 2005); fluorescently-conjugated Horse Radish Peroxidase antibody (goat HRP-cy5 1:50; Dylight 649, Jackson Laboratories); presynaptic active zone Bruchpilot NC82 antibody (mouse anti-BRP, 1:200; University of Iowa Developmental Studies Hybridoma Bank (DSHB); Buchner et al., 1988; Wagh et al., 2006); membrane scaffold Discs Large antibody (mouse anti-DLG, 1:200; DSHB; Parnas et al., 2001); GluRIIA subunit 8B4D2 antibody [mouse anti-GluRIIA, 1:100; DSHB; (Marrus et al., 2004), originally developed by Christoph Schuster (Max Planck Gesellschaft, Tubingen, Germany) and Corey Goodman (Renovis, San Francisco, CA)]; and affinity-purified GluRIIB and GluRIIC subunit antibodies (both rabbit, anti-GluRIIB 1:2500, anti-GluRIIC 1:500; Marrus et al., 2004). Primary antibodies were incubated overnight at 4℃

and washed 3×20 minutes at RT. Secondary antibodies were incubated 2 hours at RT and washed 3×20 minutes at RT (Alexa 488; goat anti-Mouse 1:250, goat anti-Rabbit 1:250; Alexa 568; goat anti-Mouse, goat anti-Rabbit 1:250; Invitrogen). Experimental and control samples for each trial were dissected and processed identically in the same dish. Ventral-longitudinal muscle 6/7 NMJs of one abdominal hemisegment A2 and A3 per animal were visualized with a Zeiss LSM 510 meta confocal microscope using LSM acquisition software. Fluorescent intensity and structural parameters were measured in ImageJ and statistical significance was assessed using InStat3 statistical software.

Western blotting

The brain and ventral nerve chord of 5–10 wandering 3rd instar larvae were homogenized in Laemilli's sample buffer (BioRad), boiled for 5 minutes, and samples were loaded onto a 4–12% Bis–Tris gel, electrophoresed (1 hour at 200 V) and transferred (1 hour at 100 V) to nitrocellulose. Membranes were blocked for 1 hour in Odyssey blocking buffer (Li-Cor, Lincoln, NE, USA) and probed for 12–16 hours at 48℃ with primary antibodies anti-LGL (1:10,000) and anti-α-Tubulin (1:400,000). Blots were washed with THAM/NaCl/NP-40 buffer and then probed for 1 hour at 25℃ with secondary antibodies. Secondary Antibodies used include: Alexa-Fluor-680-conjugated goat anti-mouse (1:10,000) and Alexa-Fluor-680-conjugated goat anti-rabbit (1:10,000) (Invitrogen-Molecular Probes, Carlsbad, CA). Blots were imaged using the Odyssey Infrared Imaging System (Li-Cor).

Electrophysiology

Two-electrode voltage-clamp (TEVC) recordings were performed from muscle of female wandering third instars, as previously described (Rohrbough et al., 1999; Long et al., 2008). Briefly, all recordings were performed at 18℃ in physiological recording saline containing 128 mM NaCl, 2 mM KCl, 4 mM $MgCl_2$, 0.5 mM $CaCl_2$, 70 mM Sucrose and 5 mM HEPES. Synaptic currents were recorded from ventral-longitudinal muscle 6 of abdominal hemisegments A23 clamped with a command voltage (V_{com}) of −60 mV (Rohrbough et al., 1999). Evoked excitatory junctional currents (EJCs) were induced with a 0.5 milliseconds suprathreshold stimulation of the severed motor nerve using a glass suction electrode. EJCs were stimulated at 0.2 Hz and sampled at 20 kHz via an Axon Instruments Digidata 1322a acquisition system, filtered with 2 kHz lowpass using Clampex 9.2 recording software. Each EJC recording session consisted of 10 evoked traces ($n=1$), with the mean amplitude measured using Clampfit 9.2 analysis software. Miniature excitatory junctional currents (mEJCs) were sampled at 10 kHz in continuous gap-free mode for 180 seconds ($n=1$) with a 500 Hz low-pass filter. mEJC frequency and amplitude were analyzed in Clampfit 9.2 using a threshold filter excluding events below 250 pA, a cutoff near background noise level. All physiological records were taken from a minimum of 6 animals per genotype, with recordings from single A2 hemisegments representing an $n=1$. Representative electrophysiology traces were exported using Microsoft Excel software, and statistical significance was assessed using InStat3 statistical software.

Lipophillic dye labeling

FM1-43 dye (10 μM; Invitrogen) was used to visualize synaptic vesicle cycling as previously described, with minor modifications (Huang et al., 2006; Vijayakrishnan et al., 2009). Briefly, control and mutant wandering third instars were dissected in parallel in the same dish in Ca^{2+}-free saline at 18℃ to ensure identical experimental conditions. Dissected preparations were incubated for 5 minutes in physiological saline containing 1.8 mM Ca^{2+}, 90 mM KCl (NaCl reduced to 40 mM to preserve osmolarity) and 10 μM FM1-43, to depolarize the presynaptic terminal and stimulate the internalization of the dye. Synaptic vesicle cycling was then blocked by 5× quick washes in Ca^{2+}-free physiological saline. Ventral-longitudinal muscle 6/7 NMJs of one abdominal hemisegment A2 and A3 per animal were visualized using a Zeiss LSM 510 meta confocal microscope ('loaded'; Vijayakrishnan et al., 2009). The same NMJ terminals were subsequently unloaded by a 2-minute incubation in 90 mM KCl, 1.8 mM Ca^{2+} physiological saline, and then once again imaged ('unloaded'; Vijayakrishnan et al., 2009). The fluorescent intensity of FM1-43 loaded and unloaded NMJs was measured in ImageJ and analyzed using InStat3 statistical software.

Statistical analysis

All data obtained from independent experiments were normalized to appropriate controls. Statistical analyses for all datasets of more than two groups were performed using either One-way ANOVA or the non-parametric Kruskal–Wallis test. Assumptions of parametric analysis were tested by the Shapiro–Wilks test for normality, and Levene's test for equal variance. In some instances, datasets were log-transformed to meet these assumptions. For post-hoc comparisons of three group datasets, the Student–Newman–Keuls pairwise analysis was used. For experiments with more than three groups, Tukey–Kramer or Dunn's (non-parametric) pairwise comparisons were used. All comparisons between two groups were performed using the Mann–Whitney non-parametric U-test or Wilcoxon matched pairs test for paired data. All data analyses were performed using the Instat3 statistical software package. A table including all pairwise comparison data may be found in supplementary material Table S1.

Acknowledgements

We are most grateful to the Bloomington Drosophila Stock Center (Indiana University) and the Developmental Studies Hybridoma Bank (University of Iowa) for essential genetic lines and antibodies, respectively. We particularly thank Daniela Zarnescu (University of Arizona) for rabbit anti-LGL and Aaron DiAntonio (Washington University School of Medicine) for rabbit anti-GluRIIB/C antibodies. This study began as collaboration with Daniela Zarnescu who initially described LGL synaptic expression and *lgl* morphology. The authors declare no competing financial interests.

Author contributions

J.S. conducted all experiments and analysed all data. K.B. guided experimental design and co-wrote the paper.

Funding

This work was supported by the National Institutes of Health (NIH) [grant numbers MH084989, MH096832 to K.B.]. Deposited in PMC for release after 12 months.

Supplementary material available online at
http://jcs.biologists.org/lookup/suppl/doi:10.1242/jcs.120139/-/DC1

References

Atwood, S. X. and Prehoda, K. E. (2009). aPKC phosphorylates Miranda to polarize fate determinants during neuroblast asymmetric cell division. *Curr. Biol.* **19**, 723-729.

Betschinger, J., Mechtler, K. and Knoblich, J. A. (2003). The Par complex directs asymmetric cell division by phosphorylating the cytoskeletal protein Lgl. *Nature* **422**, 326-330.

Betschinger, J., Eisenhaber, F. and Knoblich, J. A. (2005). Phosphorylation-induced autoinhibition regulates the cytoskeletal protein Lethal (2) giant larvae. *Curr. Biol.* **15**, 276-282.

Betschinger, J., Mechtler, K. and Knoblich, J. A. (2006). Asymmetric segregation of the tumor suppressor brat regulates self-renewal in Drosophila neural stem cells. *Cell* **124**, 1241-1253.

Bilder, D., Li, M. and Perrimon, N. (2000). Cooperative regulation of cell polarity and growth by Drosophila tumor suppressors. *Science* **289**, 113-116.

Brand, A. H. and Perrimon, N. (1993). Targeted gene expression as a means of altering cell fates and generating dominant phenotypes. *Development* **118**, 401-415.

Broadie, K., Bellen, H. J., DiAntonio, A., Littleton, J. T. and Schwarz, T. L. (1994). Absence of synaptotagmin disrupts excitation-secretion coupling during synaptic transmission. *Proc. Natl. Acad. Sci. USA* **91**, 10727-10731.

Buchner, E., Bader, R., Buchner, S., Cox, J., Emson, P. C., Flory, E., Heizmann, C. W., Hemm, S., Hofbauer, A. and Oertel, W. H. (1988). Cell-specific immuno-probes for the brain of normal and mutant Drosophila melanogaster. I. Wildtype visual system. *Cell Tissue Res.* **253**, 357-370.

Chen, K. and Featherstone, D. E. (2005). Discs-large (DLG) is clustered by presynaptic innervation and regulates postsynaptic glutamate receptor subunit composition in Drosophila. *BMC Biol.* **3**, 1.

Chung, C., Barylko, B., Leitz, J., Liu, X. and Kavalali, E. T. (2010). Acute dynamin inhibition dissects synaptic vesicle recycling pathways that drive spontaneous and evoked neurotransmission. *J. Neurosci.* **30**, 1363-1376.

Cull-Candy, S. G. and Miledi, R. (1982). Properties of miniature excitatory junctional currents at the locust nerve-muscle junction. *J. Physiol.* **326**, 527-551.

Dahan, I., Yearim, A., Touboul, Y. and Ravid, S. (2012). The tumor suppressor Lgl1 regulates NMII-A cellular distribution and focal adhesion morphology to optimize cell migration. *Mol. Biol. Cell* **23**, 591-601.

Darnell, J. C., Van Driesche, S. J., Zhang, C., Hung, K. Y. S., Mele, A., Fraser, C. E., Stone, E. F., Chen, C., Fak, J. J., Chi, S. W. et al. (2011). FMRP stalls ribosomal translocation on mRNAs linked to synaptic function and autism. *Cell* **146**, 247-261.

Davis, G. W., DiAntonio, A., Petersen, S. A. and Goodman, C. S. (1998). Postsynaptic PKA controls quantal size and reveals a retrograde signal that regulates presynaptic transmitter release in Drosophila. *Neuron* **20**, 305-315.

DiAntonio, A., Petersen, S. A., Heckmann, M. and Goodman, C. S. (1999). Glutamate receptor expression regulates quantal size and quantal content at the Drosophila neuromuscular junction. *J. Neurosci.* **19**, 3023-3032.

Dickson, B., Dietzl, G., Keleman, K. and VDRC project members (2007). RNAi construct and insertion data submitted by the Vienna Drosophila RNAi Center.

Dollar, G. L., Weber, U., Mlodzik, M. and Sokol, S. Y. (2005). Regulation of lethal giant larvae by dishevelled. *Nature* **437**, 1376-1380.

Fatt, P. and Katz, B. (1952). Spontaneous subthreshold activity at motor nerve endings. *J. Physiol.* **117**, 109-128.

Featherstone, D. E., Rushton, E., Rohrbough, J., Liebl, F., Karr, J., Sheng, Q., Rodesch, C. K. and Broadie, K. (2005). An essential Drosophila glutamate receptor subunit that functions in both central neuropil and neuromuscular junction. *J. Neurosci.* **25**, 3199-3208.

Fletcher, G. C., Lucas, E. P., Brain, R., Tournier, A. and Thompson, B. J. (2012). Positive feedback and mutual antagonism combine to polarize Crumbs in the Drosophila follicle cell epithelium. *Curr. Biol.* **22**, 1116-1122.

Fouquet, W., Owald, D., Wichmann, C., Mertel, S., Depner, H., Dyba, M., Hallermann, S., Kittel, R. J., Eimer, S. and Sigrist, S. J. (2009). Maturation of active zone assembly by Drosophila Bruchpilot. *J. Cell Biol.* **186**, 129-145.

Fredj, N. B. and Burrone, J. (2009). A resting pool of vesicles is responsible for spontaneous vesicle fusion at the synapse. *Nat. Neurosci.* **12**, 751-758.

Gateff, E. and Schneiderman, H. A. (1969). Neoplasms in mutant and cultured wild-tupe tissues of Drosophila. *Natl. Cancer Inst. Monogr.* **31**, 365-397.

Gatto, C. L. and Broadie, K. (2008). Temporal requirements of the fragile X mental retardation protein in the regulation of synaptic structure. *Development* **135**, 2637-2648.

Graf, E. R., Daniels, R. W., Burgess, R. W., Schwarz, T. L. and DiAntonio, A. (2009). Rab3 dynamically controls protein composition at active zones. *Neuron* **64**, 663-677.

Haenfler, J. M., Kuang, C. and Lee, C.-Y. (2012). Cortical aPKC kinase activity distinguishes neural stem cells from progenitor cells by ensuring asymmetric segregation of Numb. *Dev. Biol.* **365**, 219-228.

Huang, F.-D., Woodruff, E., Mohrmann, R. and Broadie, K. (2006). Rolling blackout is required for synaptic vesicle exocytosis. *J. Neurosci.* **26**, 2369-2379.

Kittel, R. J., Wichmann, C., Rasse, T. M., Fouquet, W., Schmidt, M., Schmid, A., Wagh, D. A., Pawlu, C., Kellner, R. R., Willig, K. I. et al. (2006). Bruchpilot promotes active zone assembly, Ca2+ channel clustering, and vesicle release. *Science* **312**, 1051-1054.

Korkut, C., Ataman, B., Ramachandran, P., Ashley, J., Barria, R., Gherbesi, N. and Budnik, V. (2009). Trans-synaptic transmission of vesicular Wnt signals through Evi/Wntless. *Cell* **139**, 393-404.

Long, A. A., Kim, E., Leung, H.-T., Woodruff, E., 3rd, An, L., Doerge, R. W., Pak, W. L. and Broadie, K. (2008). Presynaptic calcium channel localization and calcium-dependent synaptic vesicle exocytosis regulated by the Fuseless protein. *J. Neurosci.* **28**, 3668-3682.

Luo, L., Liao, Y. J., Jan, L. Y. and Jan, Y. N. (1994). Distinct morphogenetic functions of similar small GTPases: Drosophila Drac1 is involved in axonal outgrowth and myoblast fusion. *Genes Dev.* **8**, 1787-1802.

Mann, M. C. (1923). The occurrence and hereditary behavior of two new dominant mutations in an inbred strain of Drosophila melanogaster. *Genetics* **8**, 27-36.

Marrus, S. B., Portman, S. L., Allen, M. J., Moffat, K. G. and DiAntonio, A. (2004). Differential localization of glutamate receptor subunits at the Drosophila neuromuscular junction. *J. Neurosci.* **24**, 1406-1415.

Mathew, D., Gramates, L. S., Packard, M., Thomas, U., Bilder, D., Perrimon, N., Gorczyca, M. and Budnik, V. (2002). Recruitment of scribble to the synaptic scaffolding complex requires GUK-holder, a novel DLG binding protein. *Curr. Biol.* **12**, 531-539.

Mathew, S. S., Pozzo-Miller, L. and Hablitz, J. J. (2008). Kainate modulates presynaptic GABA release from two vesicle pools. *J. Neurosci.* **28**, 725-731.

Mechler, B. M., McGinnis, W. and Gehring, W. J. (1985). Molecular cloning of lethal(2)giant larvae, a recessive oncogene of Drosophila melanogaster. *EMBO J.* **4**, 1551-1557.

Miech, C., Pauer, H.-U., He, X. and Schwarz, T. L. (2008). Presynaptic local signaling by a canonical wingless pathway regulates development of the Drosophila neuromuscular junction. *J. Neurosci.* **28**, 10875-10884.

Mosca, T. J. and Schwarz, T. L. (2010). The nuclear import of Frizzled2-C by Importins-beta11 and alpha2 promotes postsynaptic development. *Nat. Neurosci.* **13**, 935-943.

Nitabach, M. N., Wu, Y., Sheeba, V., Lemon, W. C., Strumbos, J., Zelensky, P. K., White, B. H. and Holmes, T. C. (2006). Electrical hyperexcitation of lateral ventral pacemaker neurons desynchronizes downstream circadian oscillators in the fly circadian circuit and induces multiple behavioral periods. *J. Neurosci.* **26**, 479-489.

Ogawa, H., Ohta, N., Moon, W. and Matsuzaki, F. (2009). Protein phosphatase 2A negatively regulates aPKC signaling by modulating phosphorylation of Par-6 in Drosophila neuroblast asymmetric divisions. *J. Cell Sci.* **122**, 3242-3249.

Ohshiro, T., Yagami, T., Zhang, C. and Matsuzaki, F. (2000). Role of cortical tumour-suppressor proteins in asymmetric division of Drosophila neuroblast. *Nature* **408**, 593-596.

Pan, L. and Broadie, K. S. (2007). Drosophila fragile X mental retardation protein and metabotropic glutamate receptor A convergently regulate the synaptic ratio of ionotropic glutamate receptor subclasses. *J. Neurosci.* **27**, 12378-12389.

Parnas, D., Haghighi, A. P., Fetter, R. D., Kim, S. W. and Goodman, C. S. (2001). Regulation of postsynaptic structure and protein localization by the Rho-type guanine nucleotide exchange factor dPix. *Neuron* **32**, 415-424.

Petersen, S. A., Fetter, R. D., Noordermeer, J. N., Goodman, C. S. and DiAntonio, A. (1997). Genetic analysis of glutamate receptors in Drosophila reveals a retrograde signal regulating presynaptic transmitter release. *Neuron* **19**, 1237-1248.

Ramachandran, P., Barria, R., Ashley, J. and Budnik, V. (2009). A critical step for postsynaptic F-actin organization: regulation of Baz/Par-3 localization by aPKC and PTEN. *Dev. Neurobiol.* **69**, 583-602.

Roegiers, F., Kavaler, J., Tolwinski, N., Chou, Y.-T., Duan, H., Bejarano, F., Zitserman, D. and Lai, E. C. (2009). Frequent unanticipated alleles of lethal giant larvae in Drosophila second chromosome stocks. *Genetics* **182**, 407-410.

Rohrbough, J. and Broadie, K. (2010). Anterograde Jelly belly ligand to Alk receptor signaling at developing synapses is regulated by Mind the gap. *Development* **137**, 3523-3533.

Rohrbough, J., Pinto, S., Mihalek, R. M., Tully, T. and Broadie, K. (1999). latheo, a Drosophila gene involved in learning, regulates functional synaptic plasticity. *Neuron* **23**, 55-70.

Rolls, M. M., Albertson, R., Shih, H.-P., Lee, C.-Y. and Doe, C. Q. (2003). Drosophila aPKC regulates cell polarity and cell proliferation in neuroblasts and epithelia. *J. Cell Biol.* **163**, 1089-1098.

Sara, Y., Virmani, T., Deák, F., Liu, X. and Kavalali, E. T. (2005). An isolated pool of vesicles recycles at rest and drives spontaneous neurotransmission. *Neuron* **45**, 563-573.

Schmid, A., Hallermann, S., Kittel, R. J., Khorramshahi, O., Frölich, A. M. J., Quentin, C., Rasse, T. M., Mertel, S., Heckmann, M. and Sigrist, S. J. (2008). Activity-dependent site-specific changes of glutamate receptor composition in vivo. *Nat. Neurosci.* **11**, 659-666.

Sharma, R. P. (1973). Wingless – a new mutant in D. melanogaster. *Dros. Inf. Service* **50**, 134.

Sigrist, S. J., Thiel, P. R., Reiff, D. F. and Schuster, C. M. (2002). The postsynaptic glutamate receptor subunit DGluR-IIA mediates long-term plasticity in Drosophila. *J. Neurosci.* **22**, 7362-7372.

Tessier, C. R. and Broadie, K. (2009). Activity-dependent modulation of neural circuit synaptic connectivity. *Front Mol. Neurosci* **2**, 8.

Tessier, C. R. and Broadie, K. (2012). Molecular and genetic analysis of the Drosophila model of fragile X syndrome. *Results Probl. Cell Differ.* **54**, 119-156.

Tracey, W. D., Jr, Wilson, R. I., Laurent, G. and Benzer, S. (2003). painless, a Drosophila gene essential for nociception. *Cell* **113**, 261-273.

Vijayakrishnan, N., Woodruff, E. A., 3rd and Broadie, K. (2009). Rolling blackout is required for bulk endocytosis in non-neuronal cells and neuronal synapses. *J. Cell Sci.* **122**, 114-125.

Viquez, N. M., Füger, P., Valakh, V., Daniels, R. W., Rasse, T. M. and DiAntonio, A. (2009). PP2A and GSK-3beta act antagonistically to regulate active zone development. *J. Neurosci.* **29**, 11484-11494.

Waddington, C. H. (1940). The genetic control of wing development in Drosophila. *J. Genet.* **41**, 75-113.

Wagh, D. A., Rasse, T. M., Asan, E., Hofbauer, A., Schwenkert, I., Dürrbeck, H., Buchner, S., Dabauvalle, M.-C., Schmidt, M., Qin, G. et al. (2006). Bruchpilot, a protein with homology to ELKS/CAST, is required for structural integrity and function of synaptic active zones in Drosophila. *Neuron* **49**, 833-844.

Wang, T., Liu, Y., Xu, X.-H., Deng, C.-Y., Wu, K.-Y., Zhu, J., Fu, X.-Q., He, M. and Luo, Z.-G. (2011a). Lgl1 activation of rab10 promotes axonal membrane trafficking underlying neuronal polarization. *Dev. Cell* **21**, 431-444.

Wang, S., Yang, J., Tsai, A., Kuca, T., Sanny, J., Lee, J., Dong, K., Harden, N. and Krieger, C. (2011b). Drosophila adducin regulates Dlg phosphorylation and targeting of Dlg to the synapse and epithelial membrane. *Dev. Biol.* **357**, 392-403.

Wodarz, A., Hinz, U., Engelbert, M. and Knust, E. (1995). Expression of crumbs confers apical character on plasma membrane domains of ectodermal epithelia of Drosophila. *Cell* **82**, 67-76.

Xu, J., Pang, Z. P., Shin, O.-H. and Südhof, T. C. (2009). Synaptotagmin-1 functions as a Ca2+ sensor for spontaneous release. *Nat. Neurosci.* **12**, 759-766.

Yoshihara, M., Adolfsen, B., Galle, K. T. and Littleton, J. T. (2005). Retrograde signaling by Syt 4 induces presynaptic release and synapse-specific growth. *Science* **310**, 858-863.

Zarnescu, D. C., Jin, P., Betschinger, J., Nakamoto, M., Wang, Y., Dockendorff, T. C., Feng, Y., Jongens, T. A., Sisson, J. C., Knoblich, J. A. et al. (2005). Fragile X protein functions with lgl and the par complex in flies and mice. *Dev. Cell* **8**, 43-52.

Zhang, Y., Guo, H., Kwan, H., Wang, J.-W., Kosek, J. and Lu, B. (2007a). PAR-1 kinase phosphorylates Dlg and regulates its postsynaptic targeting at the Drosophila neuromuscular junction. *Neuron* **53**, 201-215.

Zhang, X., Zhu, J., Yang, G.-Y., Wang, Q.-J., Qian, L., Chen, Y.-M., Chen, F., Tao, Y., Hu, H.-S., Wang, T. et al. (2007b). Dishevelled promotes axon differentiation by regulating atypical protein kinase C. *Nat. Cell Biol.* **9**, 743-754.

Journal of Cell Science

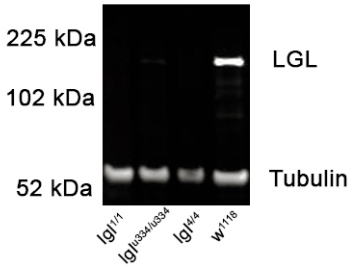

Fig. S1. Anti-LGL western blot analysis of *lgl* mutant alleles. Representative anti-LGL western blot comparing the w^{1118} genetic background control with a *lgl* mutant allelic series. The single ~110kDa band corresponding to the predicted molecular weight of LGL in the w^{1118} control is undetectable in both $lgl^{1/1}$ and $lgl^{4/4}$ mutants, but a very faint band is present in the lgl^{u334} homozygous mutant. These data are consistent with the published characterizations of the lgl^{1} and lgl^{4} alleles as protein nulls and lgl^{u334} as a hypomorphic allele (Mechler et al., 1985).

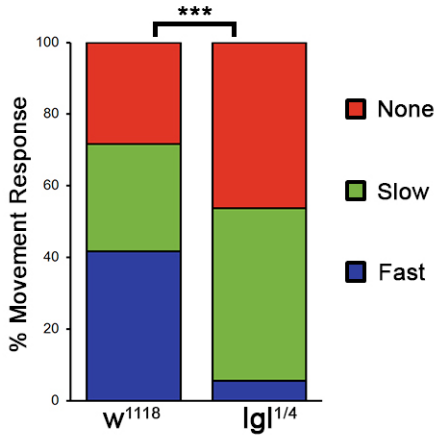

Fig. S2. Null *lgl* mutant larvae exhibit impaired behavioral movement activity. Loss of LGL reduces the coordinated motor response in a well-characterized movement escape behavior. Wandering third instars were stimulated with a 45°C probe, and movement response time assayed (see Materials and Methods). In the w^{1118} genetic background control, 42% of larvae exhibited the stereotyped escape response in ≤1 second (fast; Blue), 30% responded between 2–10 seconds (slow; Green) and 28% failed to respond (none; Red). In *lgl* nulls ($lgl^{1/4}$), only 6% initiated a fast response, 48% exhibited a delayed response, and 46% failed to respond. Statistical comparison Chi^2 test of independence ($\chi^2 = 20.004$, P<0.0001 (***); N=114, DF=2).

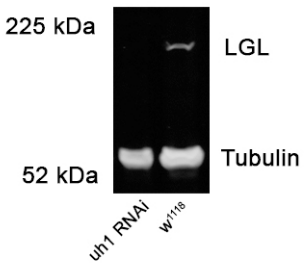

Fig. S3. Anti-LGL western blot analysis of *lgl* mutant alleles. Representative anti-LGL western blot comparing the uh1-Gal4/+ genetic background control with uh1-Gal4 × lgl RNAi. The ~110kDa band in the uh1-Gal4/+ control corresponds to the predicted molecular weight of LGL. This band is undetectable following RNAi knockdown.

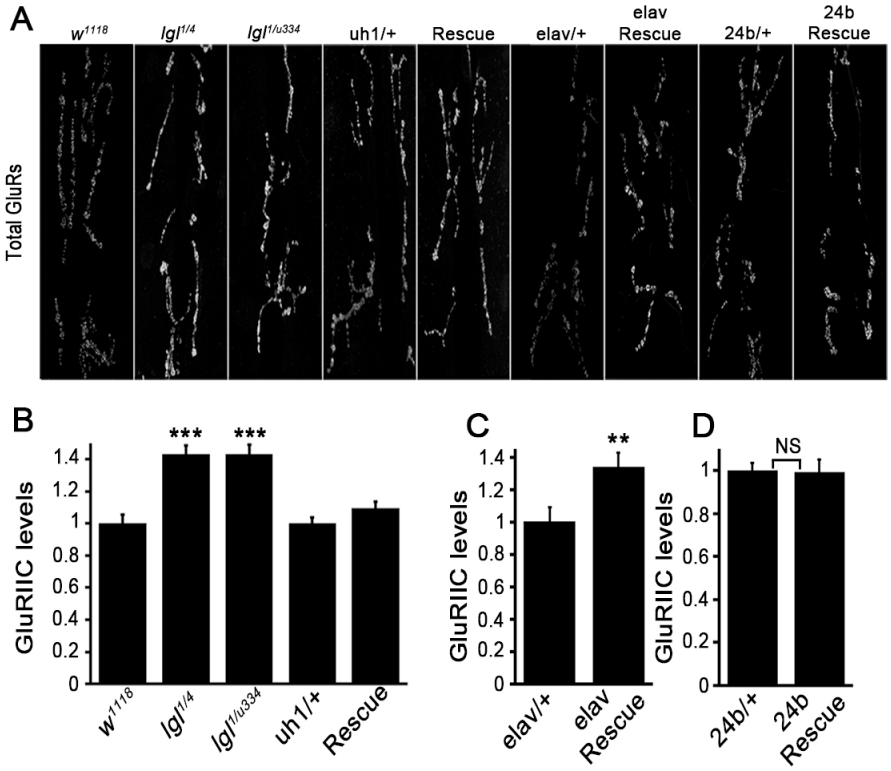

Fig. S4. High magnification image of panels A–D of Fig. 8. Loss of LGL induces a net increase in total glutamate receptors (GluRs) caused by the selective elevation of GluRIIB-containing receptors at wandering third instar NMJ synapses. (**A**) Representative muscle 6/7 NMJ images of anti-GluRIIC labeling in control (w^{1118}) and *lgl* mutant backgrounds, with ubiquitous, neuronal and muscle driven UAS-*lgl* expression. (**B**) Quantification of GluRIIC labeling intensity in w^{1118} and UAS-*lgl*/+; $lgl^{1/u334}$; uh1-Gal4/+ backgrounds compared to *lgl* mutants (N = 12, 12, 12, 13 and 13 NMJs, respectively; Kruskal–Wallis P<0.0001). (**C**) Quantification of GluRIIC intensity in the *elav*-Gal4/+ control versus UAS-*lgl* expression condition (N = 12 NMJs each; P=0.03, Mann–Whitney Test). (**D**) Quantification of GluRIIC intensity in 24b-Gal4/+ control versus UAS-*lgl*/+; $lgl^{1/u33}$; 24b-Gal4/+ condition (N=14 NMJs each; P=0.88).

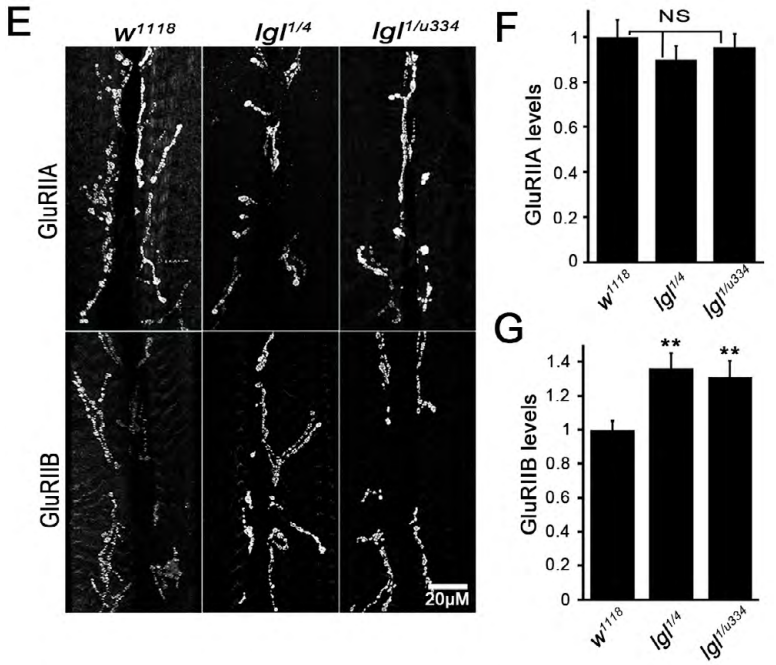

Fig. S5. High magnification image of panels E–G of Fig. 8. (**E**) Representative NMJ 6/7 images of anti-GluRIIA/B labeling in control and *lgl* mutants. (**F**) Quantification of GluRIIA intensity in control and *lgl* mutant backgrounds (N=12 NMJs each; ANOVA P=0.62, not significant (NS)). (**G**) Quantification of GluRIIB intensity in control and *lgl* mutants (N=12 NMJs each; ANOVA P=0.005). Significance shown as not significant (NS), P<0.01 (**) and P<0.001 (***).

Table S1. Post-hoc pairwise comparisons of all experiments analyzed by One-Way ANOVA. Table showing all pairwise comparisons of individual genotypes and their significance values. (**A**) Fig. 2: All results of Tukey–Kramer post-hoc tests for branch number (left) and bouton number (right). (**B**) Fig. 4: All results for Tukey–Kramer post-hoc tests for evoked junctional current responses for *lgl* mutants, rescue, and controls (left), and Student–Newman–Keuls multiple comparisons for pre- and postsynaptic LGL rescue and RNAi (right). (**C**) Fig. 5: All pairwise comparisons of *lgl* mutants, rescue, and control mEJC data. Dunn's non-parametric pairwise test for mEJC amplitude (left) and Tukey–Kramer pairwise test for mEJC frequency (right). (**D**) Fig. 6: Results of pairwise comparisons for active zone size (left) and active zone number (right) by Tukey–Kramer. (**E**) Fig. 7: Results of Student–Newman–Keuls multiple comparisons test for FM1-43 unloaded intensity (left) and unloaded/loaded ratio (right). (**F**) Fig. 8: Dunn's Multiple comparisons test of *lgl* mutants, rescue, and controls for GluRIIC intensity (left) and Student–Newman–Keuls multiple comparisons test for *lgl* mutants and control for GluRIIB intensity.

(A) Fig. 2. Structure

		Tukey–Kramer					**Tukey–Kramer**		
		Branch number					**Bouton number**		
w^{1118}	vs	$lgl^{1/4}$	***	P<0.001	w^{1118}	vs	$lgl^{1/4}$	*	P<0.05
w^{1118}	vs	lgl1/u334	**	P<0.01	w^{1118}	vs	$lgl^{1/u334}$	*	P<0.05
w^{1118}	vs	uh1-Gal4/+	ns	P>0.05	w^{1118}	vs	uh1xw	ns	P>0.05
w^{1118}	vs	uh1-Gal4 Rescue	ns	P>0.05	w^{1118}	vs	uh1-Gal4 Rescue	ns	P>0.05
$lgl^{1/4}$	vs	lgl1/u334	ns	P>0.05	$lgl^{1/4}$	vs	$lgl^{1/u334}$	ns	P>0.05
$lgl^{1/4}$	vs	uh1xw	***	P<0.001	$lgl^{1/4}$	vs	uh1-Gal4/+	*	P<0.05
$lgl^{1/4}$	vs	uh1-Gal4 Rescue	***	P<0.001	$lgl^{1/4}$	vs	uh1-Gal4 Rescue	**	P<0.01
$lgl^{1/u334}$	vs	uh1-Gal4/+	**	P<0.01	$lgl^{1/u334}$	vs	uh1-Gal4/+	*	P<0.05
$lgl^{1/u334}$	vs	uh1-Gal4 Rescue	**	P<0.01	$lgl^{1/u334}$	vs	uh1-Gal4 Rescue	**	P<0.01
uh1-Gal4/+	vs	uh1-Gal4 Rescue	ns	P>0.05	uh1-Gal4/+	vs	uh1-Gal4 Rescue	ns	P>0.05

(B) Fig. 4. EJC

		Tukey–Kramer			**Student–Newman–Kuels multiple comparisons test**				
w^{1118}	vs	$lgl^{1/u334}$	**	P<0.01	24b Rescue	vs	24b-Gal4/+	*	P<0.05
w^{1118}	vs	$lg^{lu334/u334}$	*	P<0.05	24b Rescue	vs	24b RNAi	ns	P>0.05
w^{1118}	vs	$lgl^{1/1}$	*	P<0.05	24b RNAi	vs	24b-Gal4/+	*	P<0.05
w^{1118}	vs	uh1-Gal4/+	ns	P>0.05					
w^{1118}	vs	uh1-Gal4 Rescue	ns	P>0.05	ELAV Rescue	vs	ELAV-Gal4/+	**	P<0.01
$lgl^{1/u334}$	vs	$lg^{lu334/u334}$	ns	P>0.05	ELAV Rescue	vs	ELAV RNAi	ns	P>0.05
$lgl^{1/u334}$	vs	$lgl^{1/1}$	ns	P>0.05	ELAV RNAi	vs	ELAV-Gal4/+	*	P<0.05
$lgl^{1/u334}$	vs	uh1-Gal4/+	**	P<0.01					
$lgl^{1/u334}$	vs	uh1-Gal4 Rescue	*	P<0.05					
$lg^{lu334/u334}$	vs	$lgl^{1/1}$	ns	P>0.05					
$lg^{lu334/u334}$	vs	uh1-Gal4/+	*	P<0.05					
$lg^{lu334/u334}$	vs	uh1-Gal4 Rescue	*	P<0.05					
$lgl^{1/1}$	vs	uh1-Gal4/+	*	P<0.05					
$lgl^{1/1}$	vs	uh1-Gal4 Rescue	*	P<0.05					
uh1-Gal4/+	vs	uh1-Gal4 Rescue	ns	P>0.05					

(C) Fig. 5. mEJC

Dunn's Multiple comparisons test (non-parametric)					**Tukey–Kramer**				
		Amplitude					**Frequency**		
w^{1118}	vs	$lgl^{1/u334}$	***	P<0.001	w^{1118}	vs	$lgl^{1/u334}$	***	P<0.001
w^{1118}	vs	$lg^{lu334/u334}$	**	P<0.01	w^{1118}	vs	$lg^{lu334/u334}$	***	P<0.001

w^{1118}	vs	lgl1/1	***	P<0.001	w^{1118}	vs	$lgl^{1/1}$	**	P<0.01
w^{1118}	vs	uh1-Gal4/+	ns	P>0.05	w^{1118}	vs	uh1-Gal4/+	ns	P>0.05
w^{1118}	vs	uh1-Gal4 Rescue	ns	P>0.05	w^{1118}	vs	uh1-Gal4 Rescue	ns	P>0.05
$lgl^{1/u334}$	vs	$lg^{lu334/u334}$	ns	P>0.05	$lgl^{1/u334}$	vs	$lg^{lu334/u334}$	ns	P>0.05
$lgl^{1/u334}$	vs	lgl1/1	ns	P>0.05	$lgl^{1/u334}$	vs	$lgl^{1/1}$	ns	P>0.05
$lgl^{1/u334}$	vs	uh1-Gal4/+	***	P<0.001	$lgl^{1/u334}$	vs	uh1-Gal4/+	***	P<0.001
$lgl^{1/u334}$	vs	uh1-Gal4 Rescue	**	P<0.01	$lgl^{1/u334}$	vs	uh1-Gal4 Rescue	**	P<0.01
$lg^{lu334/u334}$	vs	$lgl^{1/1}$	ns	P>0.05	$lg^{lu334/u334}$	vs	$lgl^{1/1}$	ns	P>0.05
$lg^{lu334/u334}$	vs	uh1-Gal4/+	**	P<0.01	$lg^{lu334/u334}$	vs	uh1-Gal4/+	***	P<0.001
$lg^{lu334/u334}$	vs	uh1-Gal4 Rescue	*	P<0.05	$lg^{lu334/u334}$	vs	uh1-Gal4 Rescue	**	P<0.01
$lgl^{1/1}$	vs	uh1-Gal4/+	***	P<0.001	$lgl^{1/1}$	vs	uh1-Gal4/+	**	P<0.01
$lgl^{1/1}$	vs	uh1-Gal4 Rescue	**	P<0.01	$lgl^{1/1}$	vs	uh1-Gal4 Rescue	*	P<0.05
uh1-Gal4/+	vs	uh1-Gal4 Rescue	ns	P>0.05	uh1-Gal4/+	vs	uh1-Gal4 Rescue	ns	P>0.05

(D) Fig. 6. Active zones

		Tukey–Kramer					**Tukey–Kramer**		
		Active zone size					**Active zone number**		
w^{1118}	vs	$lgl^{1/4}$	***	P<0.001	w^{1118}	vs	$lgl^{1/4}$	**	P<0.01
w^{1118}	vs	$lgl^{1/u334}$	***	P<0.01	w^{1118}	vs	$lgl^{1/u334}$	*	P<0.05
w^{1118}	vs	uh1-Gal4/+	ns	P>0.05	w^{1118}	vs	uh1-Gal4/+	ns	P>0.05
w^{1118}	vs	uh1-Gal4 Rescue	ns	P>0.05	w^{1118}	vs	uh1-Gal4 Rescue	ns	P>0.05
$lgl^{1/4}$	vs	$lgl^{1/u334}$	ns	P>0.05	$lgl^{1/4}$	vs	$lgl^{1/u334}$	ns	P>0.05
$lgl^{1/4}$	vs	uh1-Gal4/+	***	P<0.001	$lgl^{1/4}$	vs	uh1-Gal4/+	**	P<0.01
$lgl^{1/4}$	vs	uh1-Gal4 Rescue	***	P<0.001	$lgl^{1/4}$	vs	uh1-Gal4 Rescue	*	P<0.05
$lgl^{1/u334}$	vs	uh1-Gal4/+	***	P<0.001	$lgl^{1/u334}$	vs	uh1-Gal4/+	*	P<0.05
$lgl^{1/u334}$	vs	uh1-Gal4 Rescue	***	P<0.001	$lgl^{1/u334}$	vs	uh1-Gal4 Rescue	*	P<0.05
uh1-Gal4/+	vs	uh1-Gal4 Rescue	ns	P>0.05	uh1-Gal4/+	vs	uh1-Gal4 Rescue	ns	P>0.05

(E) Fig. 7. FM1-43

Student–Newman–Kuels multiple comparisons test

		Unloaded intensity					**Unloaded/loaded intensity**		
$lgl^{1/4}$	vs	w^{1118}	*	P<0.05	$lgl^{1/4}$	vs	w^{1118}	**	P<0.01
$lgl^{1/4}$	vs	$lgl^{1/u334}$	ns	P>0.05	$lgl^{1/4}$	vs	$lgl^{1/u334}$	ns	P>0.05
$lgl^{1/u334}$	vs	w^{1118}	*	P<0.05	$lgl^{1/u334}$	vs	w^{1118}	*	P<0.05

(F) Fig. 8. GluR expression

		Dunn's multiple comparisons test					**Student–Newman–Kuels multiple comparisons test**		
		GluRIIC intensity					**GluRIIB intensity**		
w^{1118}	vs	$lgl^{1/4}$	***	P<0.001	w^{1118}	vs	$lgl^{1/4}$	**	P<0.01
w^{1118}	vs	$lgl^{1/u334}$	***	P<0.01	w^{1118}	vs	$lgl^{1/u334}$	**	P<0.01
w^{1118}	vs	uh1-Gal4/+	ns	P>0.05	$lgl^{1/u334}$	vs	$lgl^{1/4}$	ns	P>0.05
w^{1118}	vs	uh1-Gal4 Rescue	ns	P>0.05					
$lgl^{1/4}$	vs	$lgl^{1/u334}$	ns	P>0.05					
$lgl^{1/4}$	vs	uh1-Gal4/+	***	P<0.001					
$lgl^{1/4}$	vs	uh1-Gal4 Rescue	*	P<0.05					
$lgl^{1/u334}$	vs	uh1-Gal4/+	***	P<0.001					

lgl$^{1/u334}$	vs	uh1-Gal4 Rescue	*	P<0.05
uh1-Gal4/+	vs	uh1-Gal4 Rescue	ns	P>0.05